

Frozen reaction fronts in steady flows: a burning-invariant-manifold perspective

John R. Mahoney,^{1,*} John Li,^{1,2} Carleen Boyer,³ Tom Solomon,³ and Kevin A. Mitchell^{1,†}

¹University of California, Merced, California 95344, USA

²University of Southern California, Los Angeles, CA 90089, USA

³Bucknell University, Lewisburg, Pennsylvania 17837, USA

(Dated: September 24, 2018)

The dynamics of fronts, such as chemical reaction fronts, propagating in two-dimensional fluid flows can be remarkably rich and varied. For time-invariant flows, the front dynamics may simplify, settling in to a steady state in which the reacted domain is static, and the front appears “frozen”. Our central result is that these frozen fronts in the two-dimensional fluid are composed of segments of *burning invariant manifolds*—invariant manifolds of front-element dynamics in $xy\theta$ -space, where θ is the front orientation. Burning invariant manifolds (BIMs) have been identified previously as important local barriers to front propagation in fluid flows. The relevance of BIMs for frozen fronts rests in their ability, under appropriate conditions, to form global barriers, separating reacted domains from nonreacted domains for all time. The second main result of this paper is an understanding of bifurcations that lead from a nonfrozen state to a frozen state, as well as bifurcations that change the topological structure of the frozen front. Though the primary results of this study apply to general fluid flows, our analysis focuses on a chain of vortices in a channel flow with an imposed wind. For this system, we present both experimental and numerical studies that support the theoretical analysis developed here.

PACS numbers: 47.70.Fw, 82.40.Ck, 47.10.Fg

I. INTRODUCTION: REACTING FLOWS AND FROZEN FRONTS

The evolution of an autocatalytic reaction $A+B \rightarrow 2A$ in a spatially-extended system is characterized by the propagation of reaction fronts that separate the species A and B . The motion of these fronts is well-understood for reaction-diffusion systems in the absence of any substrate flow. The effects of fluid motion on fronts in the more general *advection-reaction-diffusion* system have only recently received significant attention. This is somewhat surprising, given the applicability of advection-reaction-diffusion to a wide range of systems, including microfluidic chemical reactors [1], plasmas [2], the dynamics of ecosystems in the oceans (e.g., plankton blooms) [3], cellular- and embryonic-scale biological processes [4, 5], and the propagation of diseases in society [6]. It has been recently proposed that the motion of reaction fronts in fluid flows may be dominated by the presence of *burning invariant manifolds* (BIMs), which act as one-way barriers to advancing fronts [7, 8]. The existence of BIMs and their function as one-way barriers has been verified experimentally in time-independent and time-periodic vortex chain flows, as well as 2D disordered vortex flows [9].

Experiments have shown that reaction fronts tend to pin to vortex structures in the presence of an imposed wind [10]. These fronts neither propagate forward against the wind nor are blown backwards, but remain “frozen”. This behavior is surprisingly robust, occurring over more than an order of magnitude of wind speeds and

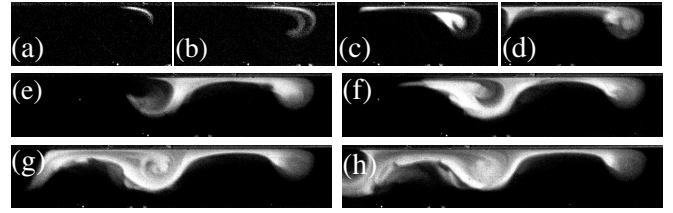


FIG. 1. Sequence showing the evolution of a triggered reaction front. The maximum fluid vortex speed (in the absence of wind) is $U = 1.4$ mm/s, and the wind speed is $V_w = 0.90$ mm/s. The images in the sequence are separated by 10 s.

a variety of underlying flows ranging from confined vortex chains to extended, spatially-random flows. Figure 1 shows a sequence of images from experiments showing the evolution of a triggered, autocatalytic reaction front in a vortex chain with wind. The front eventually stabilizes and remains fixed for the duration of the experiment.

In this paper, we use the theory of BIMs to characterize these *frozen fronts* (FFs). FFs occur when a BIM spans the entire width of the system with no changes in blocking direction, or when there is a combination of overlapping BIMs, with the same blocking directions, that together span the system. In either of these situations, the shape of the FF is determined by the shape of the BIMs responsible. We illustrate the creation of FFs and changes in their structure by increasing the wind applied to a canonical base flow (the alternating vortex chain) with a propagating chemical reaction. We present both experimental and numerical studies of this system.

This paper is organized as follows. We begin in Sec. II by presenting experiments involving reaction fronts in a

* jmahoney3@ucmerced.edu

† kmitchell@ucmerced.edu

particular quasi-two-dimensional fluid flow—the “windy alternating vortex chain”. The images in this section illustrate the behavior of FFs under an imposed wind of various strengths. Section III recalls some basic aspects of *burning invariant manifolds* (BIMs)—geometric structures that govern the progress of fronts in fluid flows—including the three-dimensional dynamics of front elements and fixed points of this system. Next, Sec. IV connects the previous two sections by showing that FFs are composed of BIM segments. Section V considers FFs in a numerical model of the experimental flow. It parallels Sec. II by increasing the applied wind and observing the resulting changes in the FFs. Here we discuss in detail the various FF topologies and the dynamical systems mechanism underlying the transitions which connect them. There are four appendices. Appendix A introduces a two-dimensional invariant surface of “sliding fronts”, which is used to prove several key results in the paper. Appendix B establishes the stability condition that frozen fronts must satisfy. Appendix C provides some technical analysis concerning the structure of frozen fronts at infinity. Finally, Appendix D examines attracting fixed points for this system.

II. EXPERIMENTS: WINDY ALTERNATING VORTEX CHAIN FLOW

The alternating vortex chain fluid flow has been the subject of much study, both theoretical and experimental. It has been used as a model of a two-dimensional cross-section of Rayleigh-Bénard (thermal) convection [11–14] and Taylor-Couette vortices [15], and can be used to model vortex chains and streets in oceanic and atmospheric flows [16, 17]. The alternating vortex chain has been used to study enhancement of long-range, fluid transport in cellular flows [18–21]. More recently, it has been used repeatedly in studies of chemical front propagation in advection-reaction-diffusion systems [7, 22–26]. Here we modify this flow by adding a uniform “wind”, creating the *windy alternating vortex chain* [10].

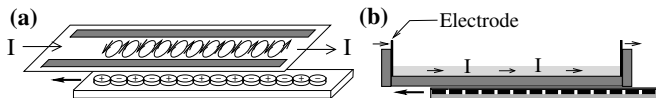


FIG. 2. Experimental apparatus. (a) Exploded view of alternating fluid vortices above array of magnets. Current through fluid induces Lorentz force. (b) Side view of the apparatus. A 2 mm thick layer of an electrolytic fluid is contained in an acrylic box. The chain of Nd-Fe-Bo magnets moves on a translation stage below the box.

A. Experimental setup

The experiments are conducted in a quasi-2D flow composed of a chain of vortices in a thin (2 mm) fluid layer. The flow is produced using a magnetohydrodynamic forcing technique, as shown in Fig. 2. A chain of permanent 1.9cm-diameter Nd-Fe-Bo magnets sits below the fluid layer, thereby imposing a spatially-varying magnetic field. An electric current is passed through this electrolytic fluid, generating Lorentz forces on the fluid. In conjunction with rigid, plastic side-walls that bound the region of interest, the result is an alternating chain of well-controlled vortices. The magnets are mounted on a translation stage; motion of the translation stage results in motion of the magnets and, consequently, the fluid vortices. In these experiments, we move the magnets (and the vortices) with a constant speed V_w . In the reference frame moving with the magnets, the flow is a stationary chain of vortices with an imposed, uniform wind of speed V_w .

The fronts are produced in the experiments with the excitable, ferroin-catalyzed Belousov-Zhabotinsky chemical reaction [27, 28]. At the beginning of an experimental run, the ferroin indicator in the solution is in its reduced (orange) state. A reaction is then triggered by briefly dipping a silver wire into the fluid. The silver oxidizes the ferroin in its vicinity, changing the local indicator to a blue-green color. The oxidized indicator in turn oxidizes the ferroin of its neighbors, resulting in a blue-green reaction front that steadily propagates outward from the trigger point with a roughly constant propagation speed V_0 . For all experiments presented in this article, the propagation speed is $V_0 = 0.07$ mm/s. The front is a pulse-like front—behind the leading edge of the front, the reaction relaxes back to its reduced (orange) state and can be re-triggered. Previous studies [24–26] have indicated that the behavior of the leading edge of these pulse-like fronts in a fluid flow is identical to the behavior of the leading edge of a burn-type reaction. (Burn-type reactions do not relax back, rather $A + B \rightarrow 2A$ and stays that way.)

B. Experimental results

We focus on the behavior of the leading edge of the reaction front that propagates *against* the imposed wind. (In the lab frame, these fronts propagate in the direction of the imposed motion of the vortex cores.) An example of a typical experiment is shown in Fig. 3. As viewed in the laboratory reference frame (Fig. 3a), the front continually propagates in both directions; in the reference frame moving with the vortices (Fig. 3b) the right-most edge of the reaction front converges to a steady-state stationary shape that remains fixed for the duration of the run. From here on, we use the expression “wind” V_w to refer to either the translational speed of the vortices in the lab frame or the speed of the uniform wind in the vortex reference frame.

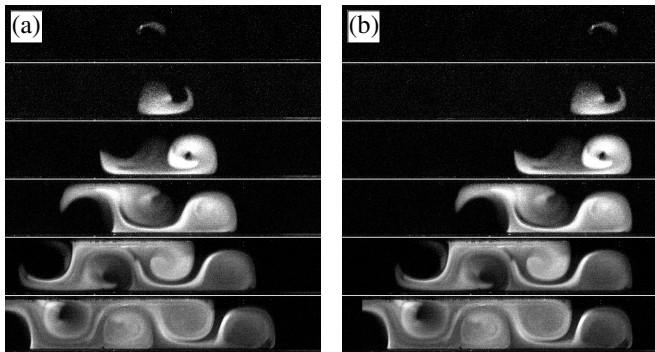


FIG. 3. Sequences showing the evolution of a reaction front in a vortex chain. (a) Lab frame, with the vortices moving to the right. (b) Reference frame moving with the vortices. In this frame, the vortices are stationary and a wind blows across the vortices toward the left. $U = 1.4$ mm/s, $V_w = 0.30$ mm/s. Images in the sequences are separated by 20 s.

The propagation of a reaction front in the alternating vortex flow in the absence of an imposed wind has been discussed in detail in previous papers [25, 26, 29, 30]. The reaction front is carried around each vortex with the flow and “burns” across the separatrix from one vortex to the next, resulting in long-range propagation that is significantly faster than the reaction-diffusion speed V_0 in a static fluid. The long-term average front speed is independent of the initial stimulation.

If a uniform wind $V_w < V_0$ is applied (i.e., the wind speed is smaller than the reaction-diffusion speed), the reaction front still propagates to the right against the wind, although the long-range propagation speed is reduced. At $V_w = V_0$, there is a transition where the front neither advances against the wind nor is blown backwards [10]. Figure 4 shows a sequence for a reaction front triggered in a flow with wind V_w just below V_0 (Fig. 4a-4c) and V_w just above V_0 (Fig. 4d-4f). The shape of the FF is not arbitrary; rather a wide range of initial stimulations will result in fronts that converge onto the same structure. For $V_w = V_0$, the shape of the FF corresponds well with the advective separatrix having $V_w = 0$.

As the strength of the imposed wind is increased, the shape of the FF evolves considerably. Figure 5 shows time-averaged images of the steady-state reaction fronts for several different wind speeds. With increasing wind speed, the contact point of the FF with the upper boundary does not move much. There is also a shift-flip symmetry apparent in Fig. 5b-5g; for every FF originating from a contact point there is a flipped version of the same structure originating from a contact point one vortex width leftward. Consequently, for any wind speed, the leading edge of the front could be pinned to any one of these contact points; i.e., any FF could be replaced by the same shape, shifted by one vortex and flipped vertically.

The shift-flip symmetry is also relevant to a change in the structure of the FF as the wind speed is increased.

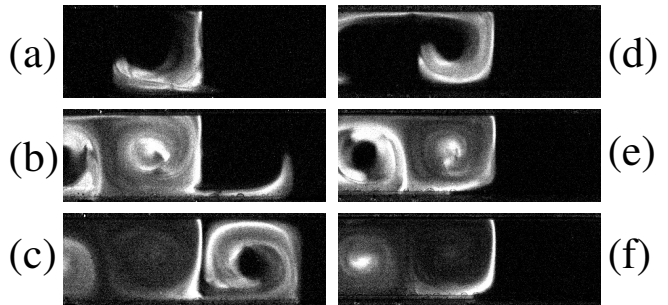


FIG. 4. Two sequences demonstrate front evolution near critical wind speed. The maximum fluid vortex speed (in the absence of wind) is $U = 0.7$ mm/s. For wind value $V_w = 0.085$ mm/s, the front is (a) nearly vertical, (b) finds a small passage into the next right vortex, and (c) fills in the right vortex continuing down the channel. For wind value $V_w = 0.090$ mm/s, the front is (d) nearly vertical, (e) does not find passage to the right, and (f) remains unchanged from (e)—a frozen front. The time between images is 40 s in both sequences. Note that there is a small amount of experimental noise that increases the transition slightly above $V_w = V_0 = 0.07$ mm/s.

The front develops a point, or corner, with an apparently discontinuous derivative (Fig. 5b). This point moves leftward for larger and larger wind speeds (Fig. 5c-5g). This concave corner first appears near the downwind contact point (one vortex width downward in Fig. 5b) and moves away from the channel wall. In this situation, the FF is composed of a combination of smooth curves that originate at different contact points.

Above a minimum wind speed, the shape of the FF is no longer uniquely determined (modulo the flip-shift symmetry); rather, more than one front shape is possible, depending on the manner in which the front is triggered (Fig. 6). It is possible to trigger a reaction front that pins only to the structure emanating from a single contact point, as in Fig. 6a. But the same flow allows for other FFs, such as in Fig. 6b. The number of different possible FF shapes increases with the wind. As can be seen in both Fig. 5 and Fig. 6, the front shapes are stretched out significantly with increasing wind speed, spanning more and more vortex cells. For all except the smallest wind speeds, a FF can be composed of structures pinned onto adjacent vortex contact points, as in Figs. 5b-5g and Figs. 6b and 6c. For larger wind speeds, additional FF shapes are possible. As an example, Fig. 6d shows a FF composed of two structures originating from contact points separated by 5 vortex widths.

Experimentally, the more complex steady-state front shapes are often found by simultaneously triggering the reaction in multiple locations. However, these complex shapes appear to be sometimes accessible with even a single, well-placed trigger. A more detailed theoretical treatment of these “basins of attraction” is in preparation.

For large enough wind, the stable state is lost completely, with the front being “blown backwards” down-

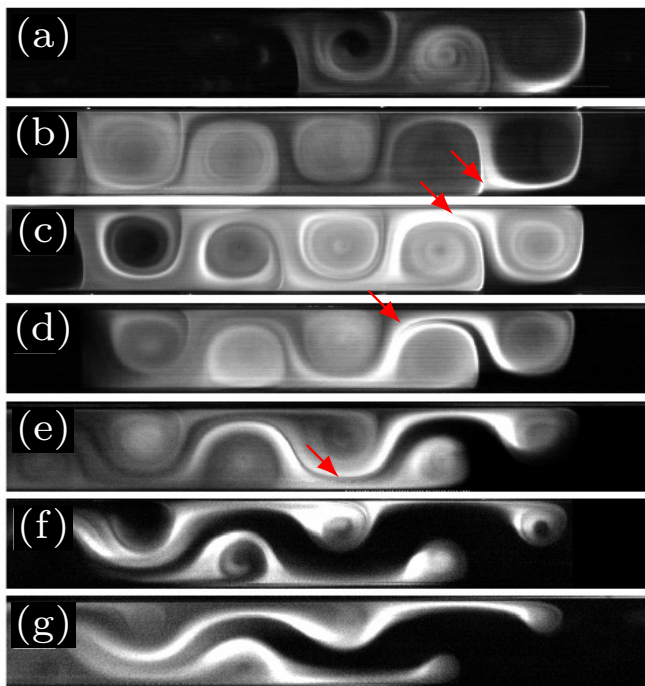


FIG. 5. (Color online.) Time-averaged images of steady-state reactions for several wind speeds. $U = 1.4$ mm/s for all. $V_w =$ (a) 0.15 mm/s, (b) 0.16 mm/s, (c) 0.20 mm/s, (d) 0.30 mm/s, (e) 0.60 mm/s, (f) 0.90 mm/s, and (g) 1.2 mm/s. Arrows indicate apparent discontinuities in the FF tangent direction.

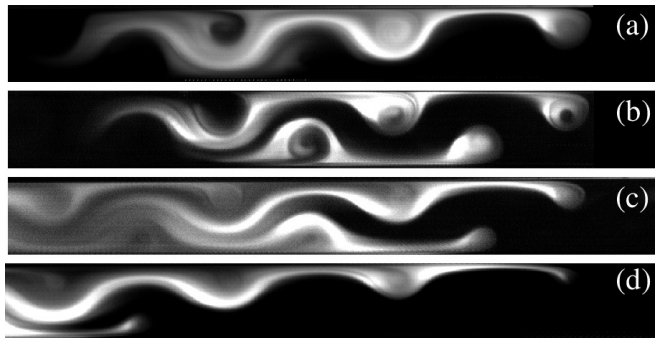


FIG. 6. Multiple FFs are realized with the same flow, depending on how the reaction is triggered. $U = 1.4$ mm/s for all. V_w is 0.90 mm/s for (a,b) and 1.2 mm/s for (c,d).

wind. A complete parameter space showing the range of wind speeds for FFs can be found in Ref. [10].

III. BIM REVIEW

We model advection-reaction-diffusion systems, such as the above experiments, by considering only the front. This amounts to taking the so-called “sharp-front”, or geometric-optics limit. While some other studies have made use of a grid-based computational scheme [23, 24],

focusing on the front is numerically economical and theoretically insightful. By assuming that the front progresses in a curvature-independent way [31], the front may be regarded as the collection of independent front elements that comprise it. Although not crucial to the basic ideas here, we also assume that the “burning speed” [32] (i.e. front propagation speed in the local fluid frame) is homogenous and isotropic.

A front is the oriented boundary of a burned region with orientation defined by the normal vector $\hat{\mathbf{n}}$ pointing away from the burned region. (We can also refer to the orientation using the tangent vector $\hat{\mathbf{g}}$ where $\hat{\mathbf{n}} \times \hat{\mathbf{g}} = +1$, i.e. pointing out of the plane.) Denoting by \mathbf{r} the xy -position of a front element and by θ the angle from the x -axis to $\hat{\mathbf{g}}$, a front is a curve in $xy\theta$ -space that satisfies the *front-compatibility criterion*,

$$\frac{d\mathbf{r}}{d\lambda} \propto \hat{\mathbf{g}}(\theta), \quad (1)$$

where λ is some smooth parameterization of the curve. The above assumptions lead to the following three-dimensional ODE governing the evolution of an individual front element $(\mathbf{r}(t), \theta(t))$.

$$\dot{\mathbf{r}} = \mathbf{u} + v_0 \hat{\mathbf{n}}, \quad (2a)$$

$$\dot{\theta} = -\hat{n}_i u_{i,j} \hat{g}_j, \quad (2b)$$

where \mathbf{u} is the prescribed fluid velocity field, which is nondimensionalized by dividing by U , the maximum fluid vortex speed in the absence of wind. That is, in the absence of wind, the maximum value of u is unity. Here, $v_0 = V_0/U$ is the nondimensionalized front propagation speed in the comoving fluid frame. The position variable \mathbf{r} is scaled so that the width of each vortex and of the channel is unity. Time is scaled by the advection time D/U , where D is the (dimensionful) vortex width. Note that $\hat{\mathbf{g}} = (\cos \theta, \sin \theta)$ and $\hat{\mathbf{n}} = (\sin \theta, -\cos \theta)$ indicate the tangent to the front element and the normal direction (propagation direction), respectively. Furthermore, $u_{i,j} = \partial u_i / \partial r_j$ and repeated indices are summed. The total translational motion of a front element is the vector sum of the fluid velocity and the front propagation velocity in the fluid frame, Eq. (2a). The change in orientation is determined entirely kinematically; Eq. (2b) describes the angular velocity of a material line embedded in the fluid.

Invariant manifolds of the full 3D ($xy\theta$) dynamics, Eq. (2), depend upon both the fluid flow and front propagation, and therefore differ from the invariant manifolds of the underlying advection dynamics. We focus on the 1D unstable manifolds attached to the burning fixed points (BFs)—i.e. fixed points of Eq. (2)—that are of stability type stable-stable-unstable (SSU). We call these *burning invariant manifolds* (BIMs). It has been demonstrated theoretically and experimentally that these BIMs are “one-way” barriers to front propagation in flows (Fig. 7). That is, they prevent reactions from crossing in one direction but allow them to cross in the

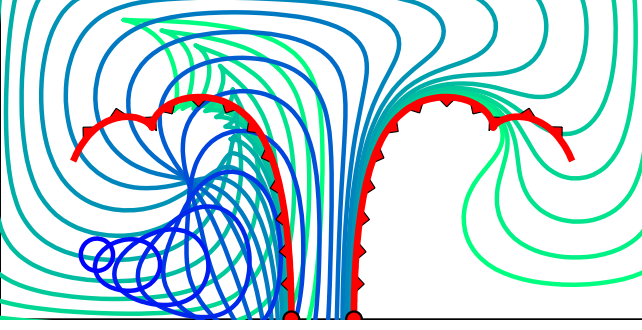


FIG. 7. (Color online.) Evolution of reaction front (blue to green) in two counter-rotating vortices. Stimulation on lower left grows while being acted on by the flow. Two BIMs (red) emanate from BFPs on the bottom channel wall. The “burning direction” of each BIM is indicated by red triangles. The reaction passes through oppositely oriented BIM, but is blocked by cooriented BIM. Finally the reaction front wraps around cusp of right BIM.

other. It is somewhat surprising that these codimension-two manifolds are in fact barriers. BIMs are not generic curves through $xy\theta$ -space; they obey the front compatibility criterion 1 [8]. All fronts, including BIMs, obey the front no-passing lemma: no front can overtake another front from behind.

An interesting consequence of the front propagation dynamics is the ability to create cusps in fronts and in the BIMs. In time-independent flows, cusps mark a change in the bounding nature of BIMs. Figure 7 illustrates the evolution of a small circular front (lower left, blue). During its evolution (blue to green), it passes through the left BIM (red) because of their opposite orientation. It then presses up against the right BIM (cooriented) and follows closely until reaching the BIM cusp where the BIM’s relative orientation changes, thus allowing passage of the reaction front. We define the *BIM core* as the BIM segment that includes the BFP and extends in both directions until reaching either a cusp, a new BFP, or infinity.

IV. FROZEN FRONTS: BASIC THEORY

Consider a fluid domain D that is connected, but not necessarily simply connected. In this paper, we focus on a channel flow where $D = \mathbb{R} \otimes [0, 1]$, but the results obtained in this section are general. We now introduce a more precise mathematical definition of frozen front than the more intuitive definition used thus far. First, we define *frozen domain* as a burned subdomain of D that is invariant under the burning dynamics and stable to perturbation [33]. (See App. B for a precise discussion of this notion of stability). Since the fluid is incompressible, neither the frozen domain nor its complement may be of finite area. A *frozen front* (FF) is the oriented boundary of a frozen domain that separates the burned from

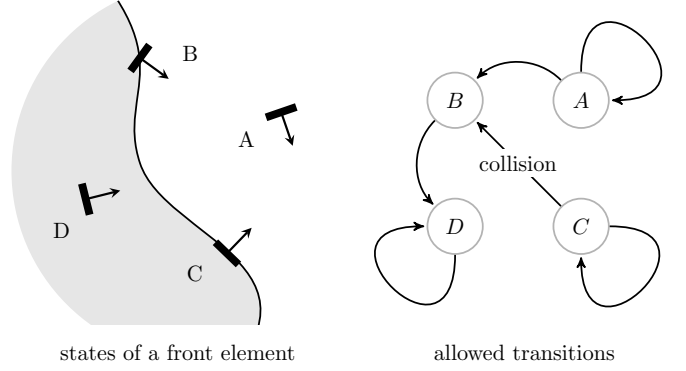


FIG. 8. An arbitrary front element exists in one of four states with respect to a burned region: A , unburned region; B , on the boundary of the burned region with non-outward-normal burning direction; C , on the boundary and oriented in the outward normal direction; D , inside the burned region. The diagram on the right indicates how the state of a front element may change as it coevolves with the burned region. These same dynamics hold between a front element and the fluid domain boundary.

the unburned fluid. (The frozen domain boundary that coincides with the boundary of D , i.e. a domain wall, is then not considered part of the frozen front.) As with any front, we choose the orientation of the FF to be a unit vector normal to the FF pointing outward from the burned region. Since the frozen domain is unbounded, the FF cannot be a closed curve.

Consider a particular FF F as a curve in $xy\theta$ -space. An individual front element on F can evolve into the interior of the frozen domain, but not vice versa (Fig. 8). Since the frozen domain is invariant, the time evolution of F under Eq. (2) includes F for any time t . In other words, the backward trajectory of any point on F remains on F . Thus the FF must be the union of segments of front element trajectories, and is hence a piece-wise smooth curve. Each segment follows a trajectory from $t = -\infty$ to some $t = t_f$. This implies each segment lies within the unstable manifold emanating from a fixed point, which may be at infinity (see App. C).

On a smooth segment of FF a front element is either a fixed point of the flow, or it “slides” along the segment satisfying $\dot{\mathbf{r}} \propto \hat{\mathbf{g}}$. Any FF can thus be decomposed into a collection of these *sliding fronts* (App. A). Here we summarize the geometry of sliding fronts detailed in App. A. First, sliding fronts only exist in the domain where $|\mathbf{u}| \geq v_0$. We refer to this domain as the fast zone FZ, and the complementary domain as the slow zone SZ. In the FZ, the structure of the sliding fronts can be simply characterized. At every point in the FZ interior, there are two allowed sliding front orientations characterized by the angle,

$$\beta = \arccos(-v_0/|\mathbf{u}|), \quad (3)$$

between the front propagation direction $\hat{\mathbf{n}}$ and the fluid flow \mathbf{u} (Fig. 9, Lemma 8). In the limit $v_0/|\mathbf{u}| \rightarrow 0$, the

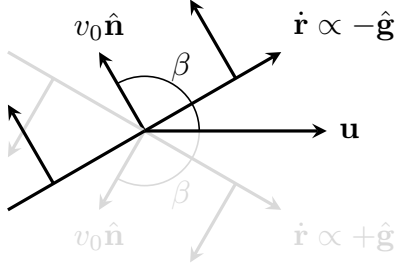


FIG. 9. A generic intersection of two sliding fronts (one black, one gray). Each sliding front's propagation vector $v_0 \hat{\mathbf{n}}$ cancels the normal component of the fluid velocity \mathbf{u} , leaving only motion tangent to the front. The two orientations (black and gray) are symmetric about \mathbf{u} .

two sliding fronts become parallel (burning in opposite directions) and align with the streamlines, thus recovering the advective case. We refer to these two choices of orientation as “+” and “−” corresponding to $\text{sgn}(\dot{\mathbf{r}} \cdot \hat{\mathbf{g}})$. Each choice of orientation defines a set of sliding fronts whose projection foliates the FZ. When the sliding fronts are considered as curves in $xy\theta$ -space, they foliate a two-dimensional surface which is a double-branched covering of the FZ. (See Figs. 23 and 24 for examples.)

Consider a burned region bounded by two sliding fronts (on different branches) that meet at a point as in Fig. 9. In principle, the burned region may be either locally concave or locally convex at this point. However, the convex case is not relevant to FFs because any convex corner will be smoothed out after an arbitrarily short evolution. Therefore, in the interior of the FZ, a FF is simply a union of smooth curves that meet at concave angles specified by the local burning-to-fluid-speed ratio $v_0/|\mathbf{u}|$. In the limit $|\mathbf{u}| \rightarrow^+ v_0$, the two branches meet on the boundary of the SZ. At all such points of the boundary, two sliding fronts meet with burning directions $\hat{\mathbf{n}}$ aligned. There are two cases to consider.

In the first case, assume $\hat{\mathbf{n}}$ is not perpendicular to the SZ. Then the sliding front trajectory passes through the fold joining the two branches in such a way that it forms a cusp in the xy -plane (Fig. 10). We observed above that cusps mark a change in the bounding behavior of BIMs. This change occurs at cusps along any sliding front (including BIMs), which implies that *a FF cannot contain a cusp*. Figure 11 illustrates why; it shows the two possible burned regions that would be bounded by such a cusp. In both cases, one segment of the sliding front has a burning direction incompatible with, i.e. pointing into, the proposed burned region.

Referring to Fig. 12, as $\hat{\mathbf{n}}$ becomes perpendicular to the SZ at the point \mathbf{x} , the cusp becomes tangent to the SZ. By symmetry, a cusp also approaches \mathbf{x} from the other side.

In the second case, where $\hat{\mathbf{n}}$ is perpendicular to the SZ, Ref. [8] showed that the sliding front must meet the SZ at a BFP \mathbf{x} . This could be thought of as the meeting of two cusps (Fig. 12). Each segment of the cusp on the left

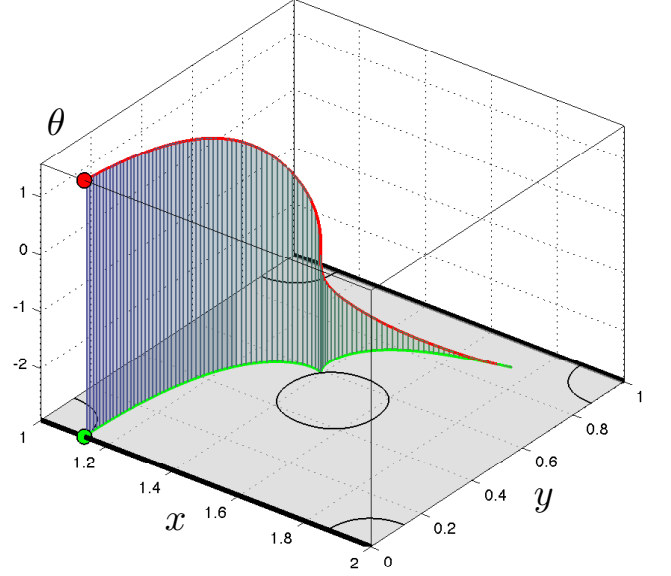


FIG. 10. (Color online.) The BIM (red) is a smooth curve in $xy\theta$ -space. Its projection (green) onto the xy -plane has a cusp on the boundary of the SZ.

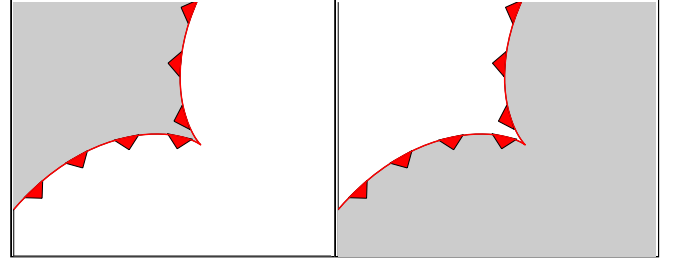


FIG. 11. (Color online.) A sliding front (red) with a cusp cannot bound a burned region (gray). Either choice of shading leads to an incompatibility in front orientation in which one piece of the front points into the burned region.

pairs with its symmetric segment on the right to form a smooth curve in xy -space passing through \mathbf{x} . Each of these two combined curves is a 1D stable or unstable manifold of \mathbf{x} . There are four possible stability types of BFPs in $xy\theta$ -space: SSS, SSU, SUU, and UUU. These are illustrated in Fig. 25. For SSU and SUU BFPs, the dynamics restricted to the sliding surface is of stability SU (Lemma 1). Figure 25 illustrates the 1D stable and unstable manifolds attached to such BFPs. For SSS and UUU points, the dynamics within the constraint surface is of stability SS and UU respectively (Lemma 1). Since the BFP is either a sink or source in this case, it is met by an infinite number of sliding trajectories.

Only two of the four stability types can occur on a frozen front. Suppose a frozen front is tangent to a SZ at a BFP where the burning direction is into the SZ, as for SUU or UUU stability types. Though the burned region behind the BFP does not intersect the SZ, a small

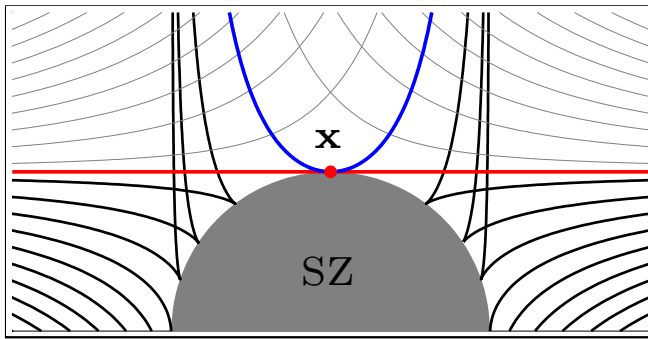


FIG. 12. (Color online.) Sliding fronts (black) strike the SZ, forming cusps on either side of an SSU BFP \mathbf{x} . As the cusps on either side approach \mathbf{x} , they become more horizontal, eventually joining tangent to each other at \mathbf{x} .

perturbation of the burned region at the BFP can intersect the SZ. Once any of the SZ is burned, the entirety of the SZ must eventually be burned and remain burned forever (Lemma 2). Since we require frozen fronts to be stable under small perturbations (App. B), SSU and UUU BFPs cannot occur on a FF.

The two remaining stability types SSU and SSS can exist on a FF. We previously showed that the FF consists of unstable manifolds. Only the SSU points have unstable manifolds. Finally, since cusps are not allowed on FFs (shown earlier), we have one of the main results of this paper.

Proposition 1. *Frozen fronts are built from BIM cores. More precisely, each frozen front is generated by some set \mathcal{S}_{FF} of SSU BFPs. The frozen front is obtained by tracing the unstable manifold from each point in \mathcal{S}_{FF} until one of three things occurs: it intersects any other BIM core emanating from \mathcal{S}_{FF} ; it intersects any domain boundary; or it terminates at an SSS BFP.*

So far we have focused our attention on the generation of the FF from BFPs. Here we shift our attention to consider how the sliding segments of a FF end. We have already discussed the most common case where segments intersect at a concave corner. There exist two other possibilities, termination on an SSU or SSS BFP.

An SSU BFP has a stable manifold that contains an *incoming* sliding front. A FF can therefore contain a segment which is a heteroclinic connection consisting of a sliding front between SSU points. Figure 13b shows two SSU BFPs joined by such a connection flowing from the upper to the lower BFP. This configuration is a FF; in particular, it is stable to perturbations of the burned region (App. B). In one sense, the FF is also structurally stable because generic perturbations of the flow yield frozen domains with a similar shape (Figs. 13a and 13c). In another sense, it is not structurally stable, because generic perturbations break the heteroclinic connection, thus altering the dynamics along the front. Some of these perturbations cause the lower SSU BFP to fall behind the FF (Fig. 13a), while other perturbations cause it to

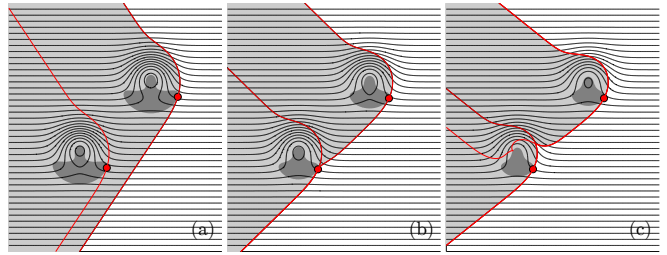


FIG. 13. (Color online.) The SSU-SSU connection is not structurally stable as the wind speed is varied. Nevertheless, the frozen domain (light gray) varies continuously. SZs are dark gray. (a) The relation $v_w < v_c$ places the lower SSU point behind the FF attached to the upper SSU point. (b) The equality $v_w = v_c$ makes the unstable manifold from the upper SSU point coincide with the stable manifold of the lower point. (c) The relation $v_w > v_c$ pushes the lower SSU point ahead, placing it and its BIM on the FF. The FF is now composed of two BIMs meeting at a concave corner.

push through, and in doing so contribute a segment of unstable sliding front to the FF (Fig. 13c). As seen in Figs. 13b and 13c, both of these perturbations return the system to the generic case. So while SSU BFPs can exist as “termination points” along a FF, this is not generic.

Finally, we consider the SSU to SSS connection. The SSS point attracts all points within a 3D neighborhood and, therefore, it attracts all sliding fronts within some neighborhood on the invariant sliding surface. It might then seem that this SSS point can be on a FF containing any of these incoming sliding fronts. However, the sliding front must reach the SSS point without having formed a cusp. This can only happen if the eigenvalues of the SSS point are real (see App. D). Such SSS points do exist, albeit for what appears to be a small parameter range.

V. THEORY: WINDY ALTERNATING VORTEX CHAIN FLOW

We continue our discussion of FFs using a simple numerical model of the experimental fluid flow.

A. Numerical model

The stream function that describes the flow is

$$\Psi = \frac{1}{\pi} \sin(\pi x) \sin(\pi y) - v_w y, \quad (4)$$

where $u_x = d\Psi/dy$ and $u_y = -d\Psi/dx$. This model has been used in several previous studies, on both fluid mixing and reacting flows, yielding reasonable agreement with experiment. Our intent here is to illustrate the theory of frozen fronts for a particular fluid flow, and to reproduce basic features of the experimental flow in Sec. II.

There is a weak three-dimensional component to the vortex flow due to Ekman pumping that carries fluid to-

ward the vortex centers at the bottom of the fluid layer and up through the vortex cores [34]. This effect is not included in the model. Also, while the model has free-slip boundary conditions, this is certainly not true in the experiment. Nevertheless, the simplified free-slip model of Eq. (4) has been used successfully in modelling several experiments on passive transport and front propagation in vortex flows [14, 20, 22, 24, 25]. The last term in Eq. (4) numerically models the fluid wind observed in the moving frame of the vortices.

B. Dynamical systems analysis

We begin by considering a flow where the wind is of insufficient strength to produce a FF (Fig. 14a). The streamlines indicate that this is essentially a vortex flow, but with a sinuous, left-moving jet. In Fig. 14b a small circular stimulation (purple) is made in the lower left. This circle evolves outward to the left and right while being deformed by the flow. The rightward moving front is able to make slow progress “upwind”. Notice though that it is blocked at the vortex boundary near the bottom and middle, and must wind around through the top of the channel. In this way, the reaction continues winding rightward through the channel indefinitely (Fig. 14c).

Figure 14d illustrates all SZs (gray), SSU BFPs (red), and BIMs (red with arrows indicating the burning direction) in this system. Two of the SZs contain the elliptic advective fixed points in the vortex centers. The others contain hyperbolic advective fixed points on the channel walls. Note that the SZs are slightly offset from a square lattice. This is due to the small wind added. We show only the SSU BFPs since, as we will show (Prop. 1), they are the generators of the unstable manifolds which combine to form FFs. Each BFP lies on a SZ boundary and, because it is SSU, is oriented away from the SZ. The BIMs emanating from these BFPs are similarly oriented. Each BIM spirals into a vortex center where it forms a cusp on an elliptic SZ (i.e. a SZ that contains an elliptic advective fixed point). Only the incoming portion of the cusp is pictured because, as shown earlier, the FF cannot contain cusps, and so the remainder of the BIM will not be relevant.

Figure 14e summarizes the dynamical structures relevant to the behavior observed in Fig. 14b and 14c. The BIM core shown is responsible for blocking front propagation at the bottom and center of the channel in Fig. 14b. The transverse stability of the BIM leads to the front’s rapid convergence upon it (Fig. 14b). As the front evolves further (Fig. 14c), it reaches the cusp at the end of the BIM core and winds around it. The BIM core does not form a complete span across the channel, and thus does not form a *global* barrier to the propagation of fronts. This is the situation seen in experimental images Figs. 4a, b, c.

Now we increase the wind speed until it precisely balances the burning speed, $v_w = v_0$ (Fig. 15). Stimulat-

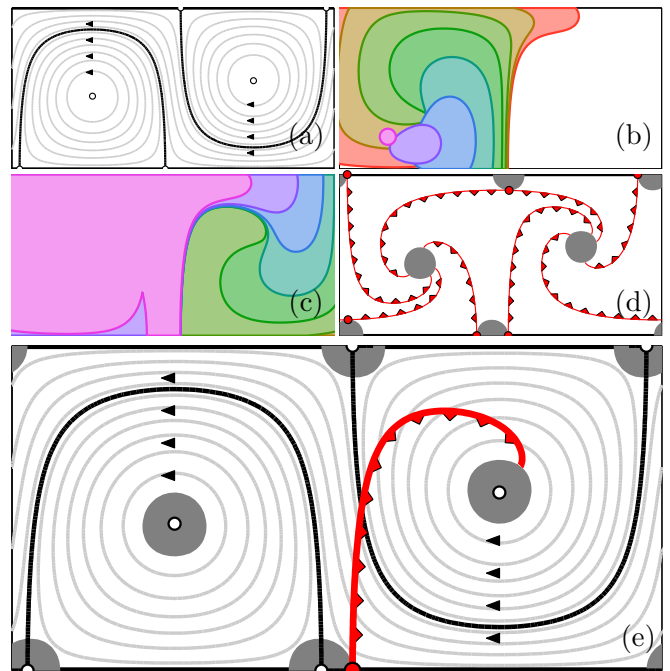


FIG. 14. (Color online.) Small wind speed ($v_0 = 0.3, v_w = 0.15$). (a) Fluid flow streamlines, fixed points and attached invariant manifolds. (b) Sequence of fronts shows preliminary convergence near bottom to roughly vertical curve. (c) Further evolution; lower edge converges to curved line while the rest proceeds around and to the right. (d) BIMs attached to BFPs. SZs shaded gray. (e) The one BIM most important for above front evolution - shown against advective structure.

ing in the lower left (purple) we find that the reaction approaches a vertical curve (Fig. 15b), and so the reaction is confined to the left side. This appears to be a candidate for a frozen domain. In Fig. 15c, we test the stability of this region by introducing a small sinusoidal perturbation. The rightward component of this perturbation grows, eventually filling in the entire cell to the right, demonstrating that this region is not stable and therefore not a frozen domain.

Let us examine the dynamical structures in Fig. 15d,e. The increase in wind has caused the SZs to shift slightly relative to Fig. 14d,e; the two on the lower boundary move together, as do the two on the upper boundary; those in the vortices move up or down depending on their rotational sense. The central BIM is now a straight vertical line. It is important to note that this BIM spans the entire channel with no cusp thus creating a *global* barrier to front propagation. Symmetry of the flow indicates that this BIM terminates at an SUU BFP at the top of the channel. We have previously argued that such a fixed point could not be on a FF, and it is this fixed point that leads to the instability demonstrated in Fig. 15c.

Now we increase the wind beyond the critical value. In Fig. 16a a stimulation on the left converges to a burned region bounded by a smooth curve spanning the channel. Unlike in Fig. 15c, a small rightward perturbation in

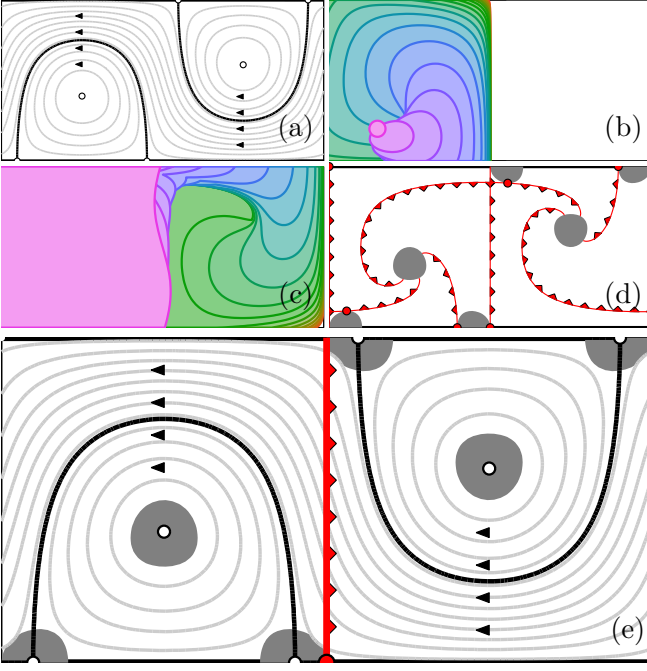


FIG. 15. (Color online.) Critical wind speed ($v_0 = v_w = 0.3$). (a) Advective structure; similar to previous case. (b) This time, front progress (from the left) is completely blocked. (c) Perturbation of burned region shows instability. (d) Several BIMs, BFPs and SZs. (e) BIM of interest is a straight vertical line - coincides with separatrix of non-windy flow.

Fig. 16b converges back to this smooth curve, and hence this curve is a FF. Figure 16c shows that the smooth bounding curve is the BIM emanating from the bottom BFP. Note that this BIM terminates at a point on the boundary that is not a BFP. This explains the situation seen in experimental images Fig. 4d, e, f as well as Fig. 5a.

Now that we have seen BIMs act as both local and global barriers, we would like to understand the transition between these two cases in more detail. Imagine a deformation that takes the BIM in Fig. 14e to the BIM in Fig. 16c; What might this deformation look like? Lemma 8 ensures that the angle between BIMs and streamlines is nonzero throughout the interior of the FZ. Therefore a BIM cannot form a tangency with the channel wall (which must coincide with a streamline) in the interior of the FZ. Note, however, that a BIM *cusp*, on the boundary of a SZ, may encounter the channel wall without forming a tangency. In fact, this occurs when the cusp is perpendicular to the channel wall (Lemma 7). This observation suggests two deformation strategies: either move the existing cusp on the elliptic SZ to the wall, or create a new cusp on the hyperbolic SZ and slide the cusp to the wall. While the first mechanism seems more straightforward, and has not been ruled out theoretically, it has not yet been observed. However, the second mechanism is observed here.

In Fig. 17 we increase v_w through the critical value $v_w = v_0$ and follow the transformation of the BIM. Be-

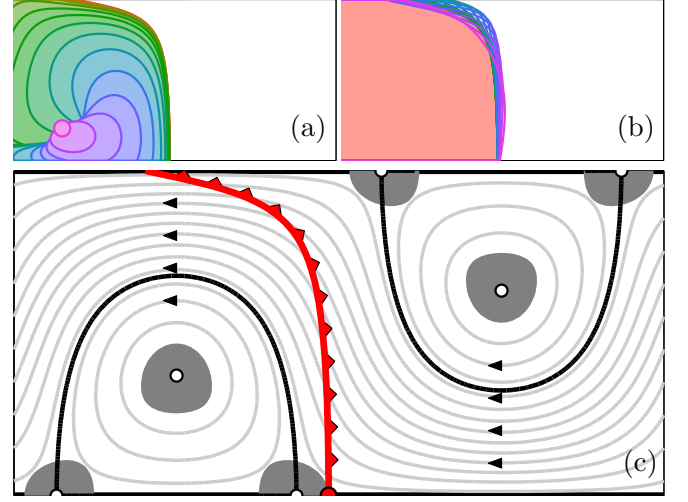


FIG. 16. (Color online.) Wind greater than critical ($v_0 = 0.3, v_w = 0.4$). A stimulation on the left (a) converges onto a smooth curve that spans the channel. In (b) a sinusoidal perturbation of this curve converges back to the curve, implying that it is stable. (Only the last front is filled). (c) The BIM responsible for the FF spans the channel with no cusps.

ginning with a subcritical v_w value in Fig. 17a, we see the BIM (green) that comes up from BFP A (not shown) on the bottom wall and veers off to the right to form a cusp on the elliptic SZ (not shown). This cusp marks the end of the BIM core.

Increasing the wind, the BIM is “blown backward” developing a tangency (red and blue dashed) with the upper SZ. This tangency is not forbidden, because the SZ is not defined by a streamline. Since the front is burning away from the SZ, the tangency must occur at either an SSU or SSS BFP on the upper SZ (according to Lemma 6 and Fig. 25.) Because the SZ is convex in this case, the BFP must be SSU. The heteroclinic connection is illustrated by the coincidence of the unstable BIM of BFP A and the stable BIM of BFP B (red and blue dashed).

Continuing to increase the wind, the BIM is blown further backward. Now it does not meet the SZ at a tangency, and so the heteroclinic connection is broken, giving way to a cusp, the other option allowed by Lemma 6. This cusp slides along the SZ, with its angle changing to remain perpendicular to the fluid flow (Lemma 6). The cusp must rotate counterclockwise, at least initially, so that its tangent points into the SZ, as rotating clockwise would require the BIM to enter the SZ.

The BIM soon arrives at another tangency with the SZ (Fig. 17b). Here, however, the BIM is burning into, rather than away from, the SZ. This tangency implies a heteroclinic connection with the SUU BFP C. (Again, the UUU case cannot occur because the SZ is convex; see Fig. 25.) In a generic three-dimensional dynamical system, heteroclinic connections between SSU and SUU fixed points are codimension-two occurrences. In this system, however, the BIMs are constrained to the two-

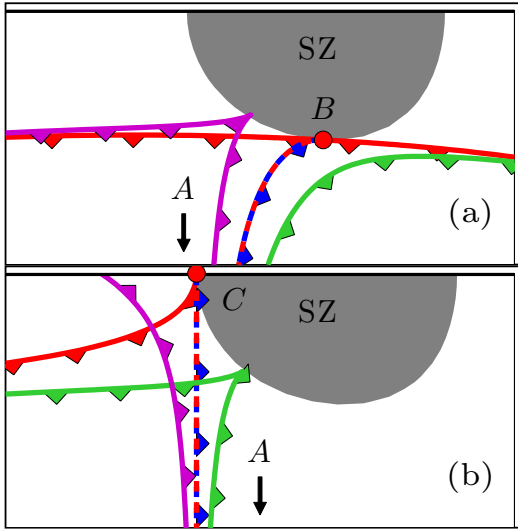


FIG. 17. (Color online.) The basic mechanism in the transition to the first FF. We increase the wind speed, showing the interplay between the BIM from BFP A (not shown) and the upper SZ and its BFPs. (a) An SSU BFP B lies on the bottom of the SZ. Attached to it are BIMs (red) going left and right, both of which end in cusps on elliptic SZs (not shown). (i) A BIM (green) comes up from the SSU BFP A below (not shown) and then shadows the unstable BIM (red) going to the right. (ii) The BIM (red and blue dashed) forms a tangency/heteroclinic connection with the BFP B . (iii) The BIM (purple) is blown behind the heteroclinic connection, forming a cusp. (b) An SUU BFP C is shown at the top of the channel. A BIM (red) lies within its unstable manifold and goes off to the left. (iv) A BIM (green) slides leftward along the SZ, approaching the BFP C . (v) The BIM (red and blue dashed) forms a second tangency/heteroclinic connection with BFP C . (vi) The BIM (purple) is blown beyond this heteroclinic connection, forming a complete span across the channel. Since the BFP positions and SZs change slightly with v_w , the specific BFPs B and C shown, as well as their SZs, are calculated for the parameter values of the heteroclinic connections.

dimensional sliding surface, and so the heteroclinic connection is a codimension-one occurrence. Said loosely, if a BIM is to sweep from one side of a SZ to the other, the BIM cannot avoid connecting with at least two BFPs on the SZ boundary.

Increasing the wind still further, the BIM, blown entirely clear of the SZ, spans the entire channel, uninterrupted by cusps. We have now arrived at the FF configuration in Fig. 16c. This FF topology persists for a significant range of wind values. As seen in Fig. 18, the shape of this front can be nearly straight, or more boomerang-shaped, depending on the applied wind. Note that it is only due to the symmetry of the flow that the second heteroclinic connection in Fig. 17b occurs exactly when the BIM core first spans the channel

At approximately wind value $v_w = 0.34 = 1.7v_0$, the BIM encounters the upper left SZ in Fig. 18. Just like the BIM/SZ transition in Fig. 17, we must form a tan-

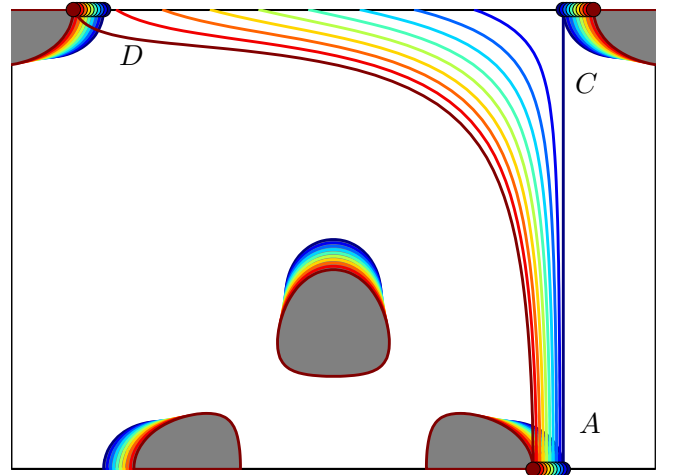


FIG. 18. (Color online.) A series of FFs for increasing wind values ($v_0 = 0.3, v_0 < v_w < 1.7v_0$, blue to red). The BIM attached to BFP A is swept backward until it intersects BFP D . The SZs also shift and are colored accordingly.

gency/heteroclinic connection (Lemma 6 and Fig. 25) to a new SSU BFP denoted BFP D . (Note the latter is rotated by roughly $\pi/2$ CCW in comparison to Fig. 17.) Foretelling this tangency, the red curves in Fig. 18 begin to curve upward near the upper channel wall. Once again, symmetry of the flow requires that BFP D be on the upper channel wall.

As v_0 is increased still further, the BIM forms a cusp just behind the unstable BIM attached to BFP D (Fig. 19b), as seen in the mechanism in Fig. 17a. Note that while a front may wrap around the newly formed cusp attempting to bypass the initial BIM, it will shortly encounter the BIM attached to BFP D which has closed off this pathway (Fig. 19a). Here we have a FF that is composed of two distinct BIMs. Note that the burning region has a concave corner, with opening angle given by Lemma 8. The appearance of this concave corner is exactly what was observed in the experimental FF (Fig. 5b).

The sequence in Fig. 20a takes the BIM through a series of encounters with SZs as the wind speed is increased. (Here we consider $v_0 = 0.2$ for simplicity.) The first encounter is the attachment/detachment mechanism with the upper right SZ, analogous to that in Fig. 17. Here, however, the BIM detachment does not result in a BIM core that spans the channel. Rather, the BIM continues for some distance and then spirals in toward the elliptic SZ in the upper left, where it forms a cusp. As the wind speed increases, the cusp slides clockwise around the SZ until the BIM forms a new tangency with the upper left SZ. The cusp on the elliptic SZ is “cut off” by this tangency, which dynamically precedes it along the BIM. This begins the mechanism of Fig. 17 again, after which the BIM core forms a complete span and defines a FF.

Figure 20b shows a similar sequence as Fig. 20a for

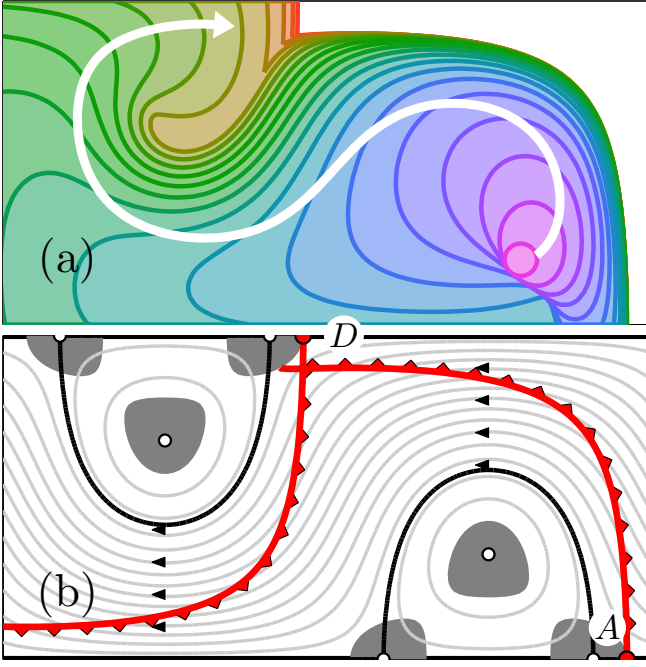


FIG. 19. (Color online.) A composite FF formed from two BIMs. ($v_0 = 0.3, v_w = 0.525$). The evolving front rapidly converges to BIM A and then winds around its cusp. However, it is prevented from going further rightward by the short segment of BIM D.

$v_0 = 0.3$. The main difference between these two images is that three SZs have merged into one in Fig. 20b. Consequently, the initial detachment of the BIM from the upper right of the SZ results in a new cusp formed near the bottom of the same SZ. Furthermore, as the cusp moves clockwise around the SZ, it is never “cut off”, but instead slides along the SZ to the channel wall.

By flip-shift symmetry of the flow, the BIM attached to BFP D has undergone the same transition as the BIM attached to BFP A and so forms a FF as well (Fig. 21a). Importantly these two FFs intersect. Consequently, in addition to the frozen domains defined by single BIMs, the *union* of two neighboring frozen domains defines a distinct frozen domain. This union is continuously related to the frozen domain observed in Fig. 19a as v_w is increased. In Figs. 16 and 19, there is a 1-to-1 correspondence between frozen domains and vortices in the channel. Now in Fig. 21, the diversity of frozen domains (at fixed v_0 and v_w) has increased. We can have either a FF formed by a single BIM core (Fig. 21b), or by two intersecting BIM cores (Fig. 21c,d,e). Note that the diversity of FFs in Figs. 21(b-e) is produced by small changes to the initial stimulation point.

As the wind is increased, the process in Fig. 20 is repeated. The BIM slides along the upper channel wall until it encounters an SSU BFP on a SZ. It moves around the SZ until it moves completely to the left of the SZ and reconnects to the channel wall. This process occurs once for each vortex pair. After each such occurrence,

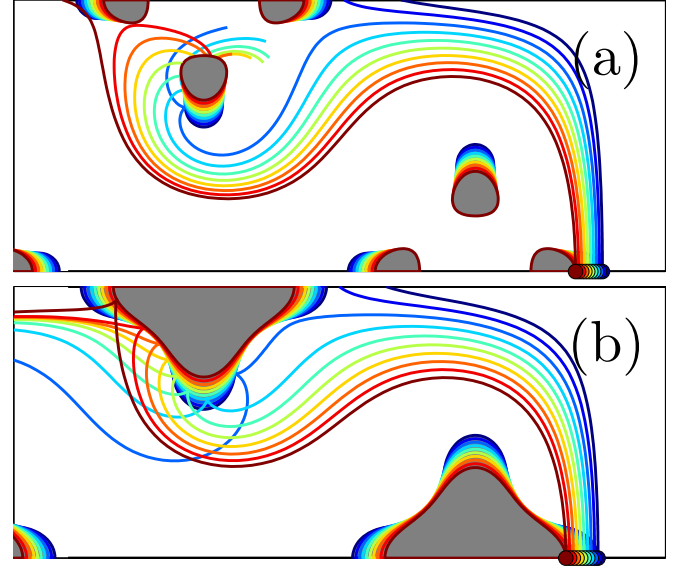


FIG. 20. (Color online.) Increasing the wind beyond first instance of FF generates new transitions. (a) ($v_0 = 0.2, 0.3 < v_w < 0.6$) Blue FF rapidly attaches to and detaches from SZ. Upon detaching, the BIM “jumps” straight to a cusp on an elliptic SZ. With even higher wind, another attachment / detachment leads again to a complete span. (b) ($v_0 = 0.3, 0.45 < v_w < 0.8$) Illustration of similar transitions where “jumping” occurs all within a single connected SZ.

the BIM acquires a new intersection with another BIM emanating from the opposite side of the channel. We can thereby enumerate all frozen domains of this system for given values of v_0 and v_w . (Fig. 22). Finally, when $\min(|\mathbf{u}|) > v_0$, there are no SZs, and therefore no BFPs, and therefore no FFs.

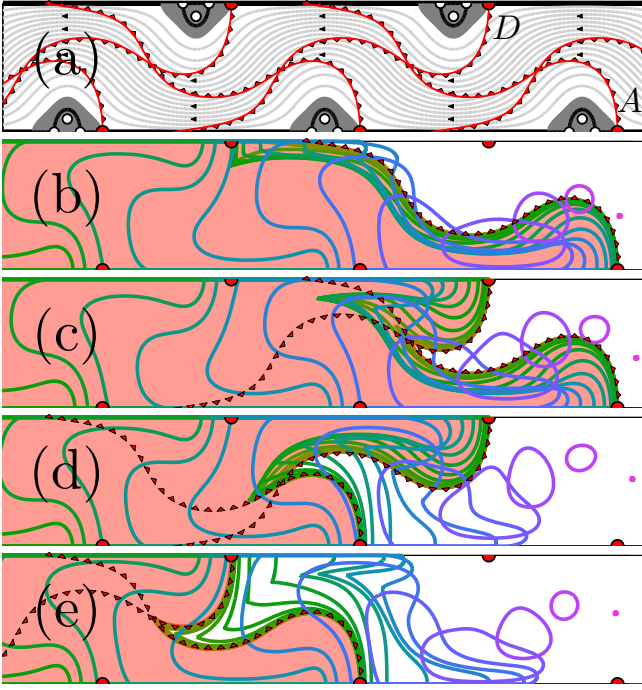


FIG. 21. (Color online.) FF diversity and sensitivity to initial stimulation. ($v_0 = 0.3, v_w = 0.95$). (a) BIMs A and D (related by flip-shift symmetry) each form a complete span, and intersect. Nearby stimulations (small pink dots near the right side) lead to different asymptotic frozen domains. The frozen domains fall into two classes: (b) and (c-e). (b) The FF is composed of a single BIM, which spans the channel. (c-e) The FF is composed of two BIMs.

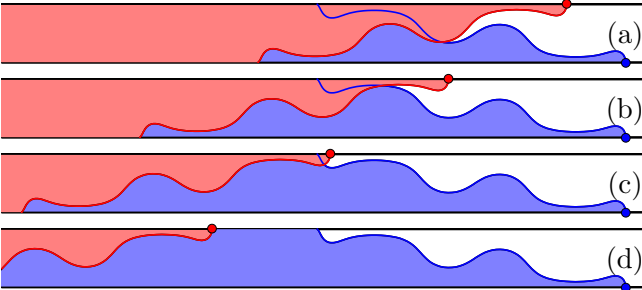


FIG. 22. (Color online.) For the windy alternating vortex chain flow we can enumerate the increasing number of possible frozen domains that occur with increasing wind speed. In this example, there are four FF shapes (up to flip-shift symmetry). ($v_0 = 0.2, v_w = 1.18$)

VI. CONCLUSIONS

The ability of a heterogeneous flow to freeze reaction fronts in the presence of an imposed wind appears to be quite general. Frozen fronts (“sustained patterns”) have been observed numerically in simulations of oceanic plankton blooms [35]. Frozen fronts have also been seen both experimentally and numerically in reacting flows in a porous media with a through-flow [36, 37]. We have also

conducted experiments on frozen fronts in extended flows composed of two-dimensional arrays of vortices, either ordered or disordered [38]. As is the case in this paper, the frozen fronts in an extended flow with a wind are due to patterns of overlapping BIMs.

This work suggests several directions of future research. In the context of design and control, this analysis could be used to develop a reacting fluid flow with some desired property. An obvious example is a system with maximal reaction rate. Given some class of accessible fluid flows, the reaction rate can be readily maximized by computing the lengths of FFs. Another example is reaction rate stability. We might be given a particular flow perturbation and seek the base flow that minimizes reaction rate fluctuation.

It may be desirable to generate a FF with a particular geometry. For instance, there may be a region in the neighborhood of the FF that we wish to keep strictly separated from the front (e.g. a sensor in the vicinity of a combustion front that cannot withstand the temperatures of the front itself). The analysis here provides a detailed connection between the stream function and FF shape making these questions accessible.

ACKNOWLEDGMENTS

The present work was supported by the US National Science Foundation under grants PHY-0748828 and CMMI-1201236 (Mitchell) and grants DMR-1004744, DMR-1361881 and PHY-1156964 (Solomon).

Appendix A: Sliding fronts

Although we study fronts propagating in time-independent fluid flows, the fronts themselves certainly need not be time-invariant. For instance, a fast-propagating front in a weak flow will evolve approximately as a circle of increasing radius. Loosely speaking, this is because each front element in the circle “burns beyond itself”. For a front to be time-invariant, each element must instead “slide along itself”. In this section, we make this statement clear and derive several consequences.

Definition 1. A front element, i.e. a point in $xy\theta$ -space, is said to be sliding when $\dot{\mathbf{r}} \propto \hat{\mathbf{g}}$, where $\hat{\mathbf{g}} = [\cos \theta, \sin \theta]$. Equivalently,

$$\dot{\mathbf{r}} \cdot \hat{\mathbf{n}} = 0, \quad (\text{A1})$$

where $\hat{\mathbf{n}} = [\sin \theta, -\cos \theta]$.

While the sliding property is defined for any fluid flow, it is of most use when the flow is time-independent, as we have assumed throughout this paper and its appendices.

The “sliding” constraint Eq. (A1) is illustrated geometrically in Fig. 9. For a given xy location, there are

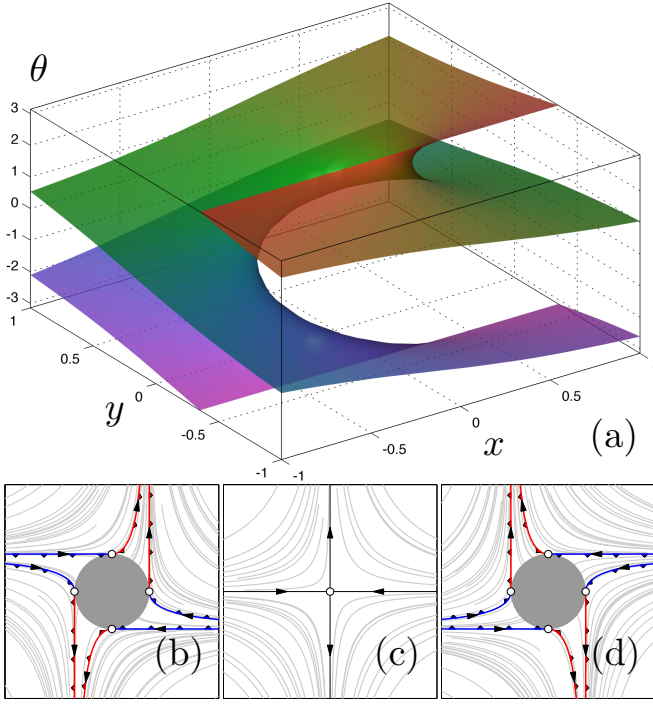


FIG. 23. (Color online.) Hyperbolic fluid flow. $\dot{\mathbf{x}} = -A\mathbf{x}, \dot{\mathbf{y}} = +A\mathbf{y}$. ($v_0 = 0.35, A = 1$) (a) Sliding surface. (b) Streamlines of the \mathbf{w}_+ field. (c) Streamlines of the advective fluid flow. (d) Streamlines of the \mathbf{w}_- field.

either zero, one or two solutions for θ satisfying this constraint. Where the fluid speed is small ($|\mathbf{u}| < v_0$), there is no solution; we call such a region a “slow zone” (SZ).

Lemma 1. *There are no sliding elements inside a SZ.*

Proof. Combining the sliding constraint Eq. (A1) with Eq. (2), we find $|\mathbf{u} \cdot \hat{\mathbf{n}}| = |v_0|$. This cannot be satisfied for $|\mathbf{u}| < v_0$. \square

Where the fluid speed is large ($|\mathbf{u}| > v_0$), there are two solutions to Eq. (A1). Where the fluid speed equals the burning speed ($|\mathbf{u}| = v_0$), these two solutions are degenerate. We call a region where $|\mathbf{u}| \geq v_0$ a “fast zone” (FZ). The sliding constraint Eq. (A1) defines a two-dimensional submanifold of $xy\theta$ -space, called the *sliding surface*, which can be viewed as a double-branched surface over the FZ. Figures 23a and 24a show the sliding surface for a hyperbolic and an elliptic flow, respectively [39]. In Figs. 23a and 24a we see that, when viewed from above, these sliding surfaces have a hole in the middle exactly where the SZ is.

Lemma 2. *If at any time some portion of a SZ is burned, the asymptotic burned domain will include that entire SZ.*

Proof. Within the SZ, the velocity of the front is everywhere greater than the fluid. Therefore, no direction of motion is forbidden to the front, and so the front will eventually access all parts of the SZ. \square

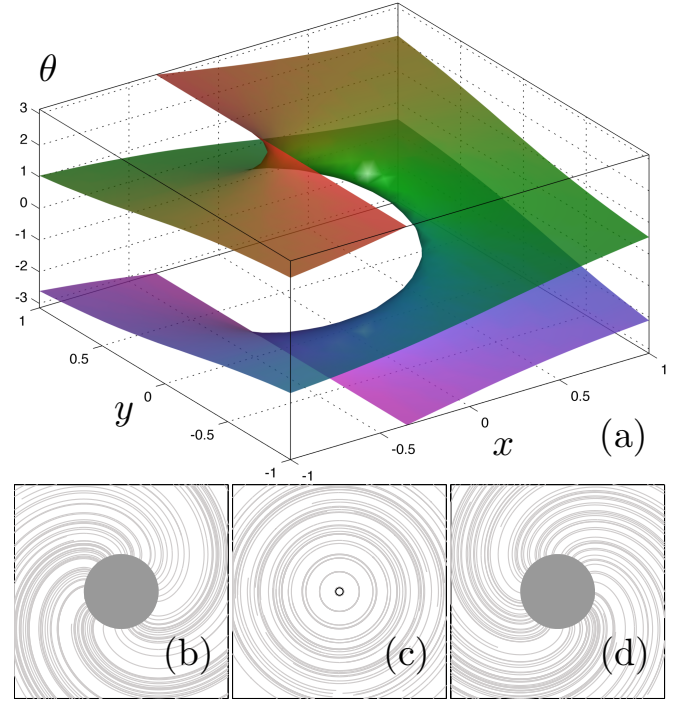


FIG. 24. (Color online.) Elliptic fluid flow. $\dot{\mathbf{x}} = -A\mathbf{y}, \dot{\mathbf{y}} = +A\mathbf{x}$. ($v_0 = 0.35, A = 1$) (a) Sliding surface. (b) Streamlines of the \mathbf{w}_+ field. (c) Streamlines of the advective fluid flow. (d) Streamlines of the \mathbf{w}_- field.

Lemma 3. *Sliding is an invariant property. That is, if a front element is sliding, every element along its trajectory under Eq. (2) is also sliding. Hence we may speak of sliding trajectories.*

Proof. We examine the time derivative of Eq. (A1).

$$\begin{aligned} \frac{d}{dt}(\dot{\mathbf{r}} \cdot \hat{\mathbf{n}}) &= (u_{i,j} \dot{r}_j + v_0 \dot{\theta} \hat{g}_i) \hat{n}_i + \dot{r}_k \hat{g}_k \dot{\theta} \\ &= \hat{n}_i u_{i,j} \dot{r}_j + \dot{r}_k \hat{g}_k \dot{\theta} \\ &= \pm |\dot{\mathbf{r}}| \hat{n}_i u_{i,j} \hat{g}_j \pm |\dot{\mathbf{r}}| \hat{g}_k \hat{g}_k \dot{\theta} \\ &= \pm |\dot{\mathbf{r}}| (-\dot{\theta}) \pm |\dot{\mathbf{r}}| \dot{\theta} = 0, \end{aligned}$$

where the first equality follows from Eq. (2a) and the fact that $d\hat{\mathbf{n}}/dt = \hat{\mathbf{g}}\dot{\theta}$, the second from the orthogonality of $\hat{\mathbf{n}}$ and $\hat{\mathbf{g}}$, the third from the sliding assumption $\dot{\mathbf{r}} = \pm |\dot{\mathbf{r}}| \hat{\mathbf{g}}$, and the fourth from Eq. (2b). \square

A consequence of this lemma is that the sliding surface is dynamically invariant.

Recall that a front is a curve $(\mathbf{r}(\lambda), \theta(\lambda))$ that everywhere satisfies the front compatibility criterion Eq. (1), which is expressed equivalently as

$$d\mathbf{r}/d\lambda \cdot \hat{\mathbf{n}} = 0. \quad (\text{A2})$$

Lemma 4. *A trajectory of Eq. (2) is sliding if and only if the curve it sweeps out is a front.*

Proof. Choosing $\lambda = t$, Eq. (A1) is equivalent to Eq. (A2). \square

In light of Lemma 4, we may refer to a sliding trajectory as a *sliding front*. More generally, we make the following definition.

Definition 2. A sliding front is a smooth curve that everywhere satisfies Eq. (A1), or equivalently Eq. (A2).

Note that a sliding front may be composed of multiple trajectories joined at fixed points. Also, any segment of a sliding front is also referred to as a sliding front.

Lemma 5. BIMs are sliding fronts, and thus lie within the sliding surface.

Proof. A BIM is the unstable invariant manifold of an SSU BFP. Since we consider time-independent flows, this invariant manifold is also a trajectory. As shown in Ref. [8], BIMs satisfy the front compatibility criterion. Therefore, by Lemma 4, BIMs are sliding fronts. \square

Since the sliding surface is invariant, it is natural to restrict Eq. (2) to this surface. We next derive an explicit expression for this 2D flow. Applying the sliding constraint Eq. (A1) to the front element dynamics Eq. (2), we have $\mathbf{u} \cdot \hat{\mathbf{n}} = -v_0$. Using this to resolve the unit vector $\hat{\mathbf{n}}$ into components, we have $\hat{\mathbf{n}} \cdot \hat{\mathbf{u}} = -v_0/|\mathbf{u}|$ and $\hat{\mathbf{n}} \cdot \hat{\mathbf{u}}^\perp = \mp \sqrt{1 - (v_0/|\mathbf{u}|)^2}$, where \mathbf{u}^\perp or $\hat{\mathbf{u}}^\perp$ is a righthanded rotation by $\pi/2$ of \mathbf{u} or $\hat{\mathbf{u}} = \mathbf{u}/|\mathbf{u}|$. Inserting the resolved form of $\hat{\mathbf{n}}$ into Eq. (2) we have,

$$\dot{\mathbf{r}} = \mathbf{w}_\pm \equiv \left[1 - \left(\frac{v_0}{|\mathbf{u}|} \right)^2 \right] \mathbf{u} \mp \frac{v_0}{|\mathbf{u}|} \sqrt{1 - \left(\frac{v_0}{|\mathbf{u}|} \right)^2} \mathbf{u}^\perp \quad (\text{A3})$$

This defines two flows over the FZ, one for each of the two branches of the sliding surface. Our sign convention is such that \mathbf{w}_+ is the flow on the branch where $\dot{\mathbf{r}} = +|\dot{\mathbf{r}}|\hat{\mathbf{g}}$ (the + branch), and \mathbf{w}_- is the flow on the branch where $\dot{\mathbf{r}} = -|\dot{\mathbf{r}}|\hat{\mathbf{g}}$ (the - branch).

Equation (A3) shows that the \mathbf{w}_\pm fields are undefined (complex-valued) within the SZ and are zero on its boundary, confirming Lemma 1. All fixed points of Eq. (2) are fixed points of Eq. (A3) because all BFPs trivially satisfy the sliding constraint. These BFPs lie on the SZ boundary. Equation (A3) also has a set of spurious fixed points at all other points along the SZ boundary, i.e. where $|\mathbf{u}| = v_0$. However, we ignore these spurious fixed points as they are not physically relevant fixed points of Eq. (2), but rather result from the square-root singularity in Eq. (A3), obtained by projecting Eq. (2) onto xy -space. This square-root singularity also invalidates the uniqueness of solutions to Eq. (A3) at the SZ boundary. Thus, there are other physically relevant trajectories that pass through the SZ boundary.

Figures 23b,d and 24b,d illustrate the \mathbf{w}_\pm flows for the cases of hyperbolic and elliptic fluid flow, respectively. The gray regions are the SZs. BFPs are indicated on the

boundary of the hyperbolic SZ. The stable and unstable manifolds of these BFPs are shown in blue and red, respectively.

Reference [8] proved that for any BFP, $\hat{\mathbf{g}}$ is an eigenvector of $u_{i,j}$, i.e.

$$u_{i,j} \hat{g}_j = \mu \hat{g}_i, \quad (\text{A4})$$

where μ is the eigenvalue. Reference [8] also defined the quantity μ' ,

$$\mu' = \mu + v_0 \kappa, \quad (\text{A5})$$

where κ is the signed curvature of the SZ boundary at the BFP. ($\kappa < 0$ means that $\hat{\mathbf{n}}$ points toward the center of curvature.) Below, we reproduce Theorem 4 from Ref. [8], [40]

Theorem 1. For a time-independent, incompressible flow \mathbf{u} , the eigenvalues about a BFP are

$$\lambda_0 = -\mu, \quad (\text{A6})$$

$$\lambda_\pm = \frac{1}{2} \left(-\mu \pm \sqrt{\mu^2 + 4\mu\mu'} \right), \quad (\text{A7})$$

where μ and μ' are given by Eqs. (A4) and (A5). The linear stability of a BFP is thus determined by the signs of μ and μ' according to the following table.

	$\mu > 0$	$\mu < 0$
$\mu' > 0$	SUS	UUU
$\mu' < 0$	SSS	SUU

We next specialize this result to the dynamics on the sliding surface.

Corollary 1. The eigenvalues for a BFP of the dynamics Eq. (2) restricted to the sliding surface are given by λ_\pm from Eq. (A7). The xy -projection of each of the corresponding eigenvectors is proportional to $\hat{\mathbf{g}}$.

The sliding surface stability information is summarized in Fig. 25. For each of the four stability types, the first two stabilities (in bold) describe the dynamics within the invariant sliding surface. Equation A5 places restrictions on the local convexity of the SZ at the BFP. These possibilities are illustrated in Fig. 25.

Lemma 6. At an intersection \mathbf{p} between a sliding front and the boundary of a SZ, the fluid flow is perpendicular to the sliding front. If the sliding front is tangent to the boundary, \mathbf{p} is a BFP. Otherwise, \mathbf{p} is a cusp along the sliding trajectory. All BFPs and cusps of sliding fronts occur at the intersection between a sliding front and SZ boundary.

Proof. Combining the sliding constraint Eq. (A1) with the front element dynamics Eq. (2) gives $\mathbf{u} \cdot \hat{\mathbf{n}} = -v_0$. Since $|\mathbf{u}| = v_0$ on the SZ boundary, $\mathbf{u} = -v_0 \hat{\mathbf{n}}$. Thus \mathbf{u} is perpendicular to $\hat{\mathbf{g}}$.

In Thm. 2 of Ref. [8], it was shown that a necessary and sufficient condition for a BFP was for it to be on the

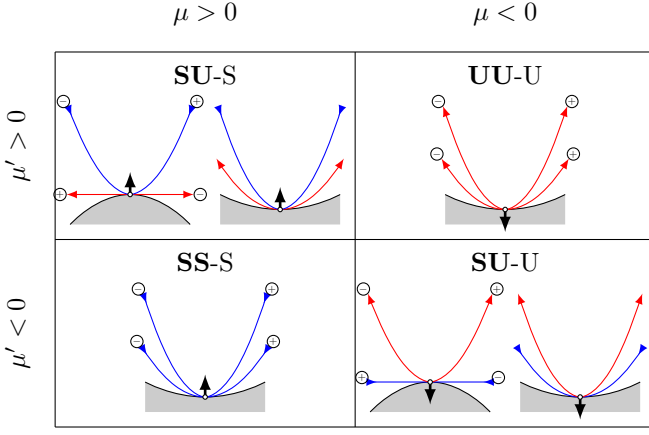


FIG. 25. (Color online.) Four BFP stability types. Black arrow indicates burning direction. Gray regions are SZs. Two un/stable manifolds of each BFP are within the sliding surface. Each manifold is labeled with $+/-$ indicating its corresponding branch of the sliding surface.

boundary of the SZ with $\hat{\mathbf{n}}$ perpendicular to the boundary. Thus $\hat{\mathbf{g}}$ tangent to the boundary implies a BFP.

If $\hat{\mathbf{g}}$ is not tangent to the boundary, then since the sliding trajectory cannot enter the SZ, it reaches the boundary and then must reverse direction forming a cusp.

Finally, a BFP and cusp both require $\dot{\mathbf{r}} = 0$. This satisfies the sliding constraint and also implies $|\mathbf{u}| = v_0$. \square

Lemma 7. *A BFP or cusp on the boundary of the fluid domain, i.e. at a wall, must have $\hat{\mathbf{g}}$ perpendicular to that boundary.*

Proof. This follows from the previous Lemma 6 and that the fluid velocity of an incompressible fluid is tangent to the fluid domain boundary. \square

An incompressible 2D fluid flow can be specified by a stream function $\Psi(\mathbf{r})$, with $u_x = d\Psi/dy$, $u_y = -d\Psi/dx$. Each fluid element follows a level set, or streamline, of Ψ . Front elements, on the other hand, do not follow streamlines, but generally cross them one way or the other depending on their relative orientation.

Lemma 8. *Sliding fronts cross streamlines such that $\theta_{\hat{\mathbf{n}}, \mathbf{u}}$, the angle between $\hat{\mathbf{n}}$ and \mathbf{u} , satisfies $\cos(\theta_{\hat{\mathbf{n}}, \mathbf{u}}) = -v_0/|\mathbf{u}|$.*

Proof. From Eq. (2), $\mathbf{u} = \dot{\mathbf{r}} - v_0\hat{\mathbf{n}}$. The sliding front condition implies $\mathbf{u} = \pm|\dot{\mathbf{r}}|\hat{\mathbf{g}} - v_0\hat{\mathbf{n}}$. Dotting with $\hat{\mathbf{n}}$, $\hat{\mathbf{n}} \cdot \mathbf{u} = -v_0$. \square

Lemma 8 means that sliding fronts are never tangent to streamlines, except in the $v_0/|\mathbf{u}| \rightarrow 0$ limit. Physical boundaries of the fluid (channel walls) are particularly important streamlines at which this lemma can be utilized.

In addition to the angle at which sliding fronts cross streamlines, we can examine how rapidly they are

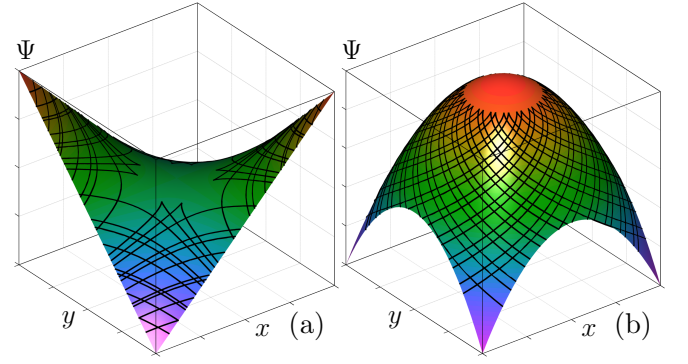


FIG. 26. (Color online.) Sliding fronts represented on the graph of the stream function Ψ near: (a) a hyperbolic point, (b) an elliptic point. Sliding fronts are curves of constant increase (or decrease) in the value of the stream function.

crossed. To this end, we calculate the rate at which Ψ changes when viewed from the frame of an individual front element.

$$\frac{D\Psi}{Dt} \equiv \frac{\partial\Psi}{\partial x} \frac{\partial x}{\partial t} + \frac{\partial\Psi}{\partial y} \frac{\partial y}{\partial t} + \frac{\partial\Psi}{\partial t} \quad (\text{A8})$$

$$= -u_y \dot{x} + u_x \dot{y} \quad (\text{A9})$$

$$= -(\dot{y} + v_0 \cos \theta) \dot{x} + (\dot{x} - v_0 \sin \theta) \dot{y} \quad (\text{A10})$$

$$= -v_0 \dot{\mathbf{r}} \cdot \hat{\mathbf{g}} \quad (\text{A11})$$

$$= -\text{sgn}(\dot{\mathbf{r}} \cdot \hat{\mathbf{g}}) v_0 |\dot{\mathbf{r}}|, \quad (\text{A12})$$

where the last equality makes use of the sliding constraint. Scaling by the front element speed, we find the simple relation

$$\frac{D\Psi}{Ds} = -\text{sgn}(\dot{\mathbf{r}} \cdot \hat{\mathbf{g}}) v_0, \quad (\text{A13})$$

where s measures the euclidean xy -length along the trajectory. Equation (A13) shows that the sliding trajectories on the $+$ ($-$) branch of the sliding surface are those that climb the stream function with the constant rate of descent (ascent) v_0 . It is straightforward to show that the only front elements that ascend or descend at a constant rate are sliding.

Consider two streamlines with values Ψ_a and Ψ_b and a sliding front $F_{a,b}$ that connects one to the other with no intervening cusps. The xy -length of the segment $F_{a,b}$ follows directly from Eq. (A13),

$$|F_{a,b}| = \frac{|\Psi_b - \Psi_a|}{v_0} \quad (\text{A14})$$

This expression is particularly useful when thinking about FFs in channel flows of arbitrary geometry. Since the channel wall enforces a boundary condition of constant Ψ , the FF length is found through Eq. (A14). Thus the length of a FF that spans a channel depends only on this “energy difference” between the two walls and the burning speed, and not on other details of the flow. While Eq. (A14) was derived for a single sliding front,

it also holds for FFs that are composed of multiple BIM cores. This can be seen by applying Eq. (A14) to each BIM segment separately. Interestingly, this implies that multiple FFs existing in the same flow must have the same length, even in the absence of any flow symmetry.

Equation (A14) also implies that a channel of width W cannot support a FF if $\Delta\Psi < v_0 W$. Furthermore, if we assume that a flow \mathbf{u} *without* wind gives no net flow down the channel, then for the flow $\mathbf{u} + \mathbf{v}_w$, Eq. (A14) becomes

$$|F_{a,b}| = W v_w / v_0. \quad (\text{A15})$$

This can be interpreted as the equality of fluid flux across the FF and across the channel width. Eq. (A15) shows that $v_w \geq v_0$ is necessary but not sufficient. In the case that FFs do occur at $v_w = v_0$, they must be straight lines that meet the channel walls at right angles. This occurs exactly when the original fluid flow ($v_w = 0$) has a vertical advective separatrix. This condition is met for the windy alternating vortex chain model; additionally Ref. [10] experimentally demonstrated that $v_w = v_0$ marked the onset of FFs. However, it is not difficult to construct flows where $v_w = v_0$ is not sufficient for the existence of FFs.

Appendix B: Stability of Frozen Domains

At the beginning of Sec. IV, we specified that frozen domains should be stable under small perturbations. Here, we define this stability more precisely. For a given invariant burned domain, with boundary F , we define an *allowable* distortion of F at a point $\mathbf{r} \in F$ to be a distortion such that F remains unchanged outside a ball of radius $\epsilon(\mathbf{r}) > 0$ centered at \mathbf{r} . Note that the value of $\epsilon(\mathbf{r})$ is not fixed but may vary with the point \mathbf{r} .

Definition 3 (Stability of frozen domains/fronts). *A frozen domain/front is required to be stable in the following sense. There must exist a function $\epsilon(\mathbf{r})$ of each point \mathbf{r} along the front F , i.e. the domain boundary, such that after any allowable distortion, the front remains pointwise close to F and converges pointwise to F as time goes to infinity.*

Here pointwise close is in the “Lyapunov” sense, in that the maximum (over all time) distance from the time-evolved distorted front to the original front F remains bounded and goes to zero as ϵ goes to zero.

With this definition, one can easily verify the argument of Sec. IV proving that a FF cannot contain an SUU or UUU BFP. One also sees that a FF can contain an SSU or SSS BFP, and that the curves constructed in Prop. 1 are stable. Regarding the latter, it is interesting to note how a perturbation of the FF F returns to F . First, a perturbation localized to the neighborhood of an SSS point simply shrinks in size, back into the original FF, due to the SSS point’s being a sink. Consider now

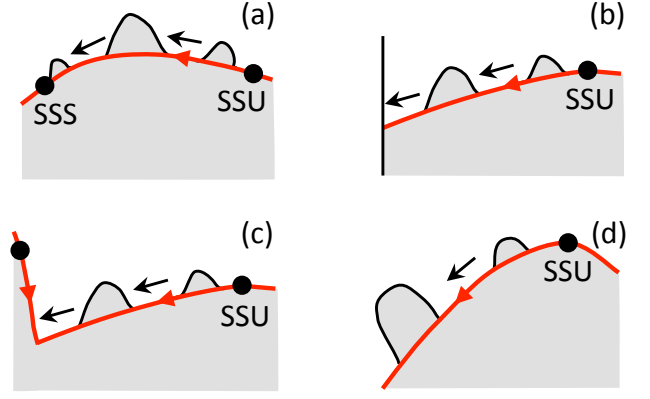


FIG. 27. (Color online.) The fates of localized perturbations to a FF. a) The perturbation eventually shrinks into an SSS BFP on the FF. b) The perturbation strikes a wall of the fluid domain. c) The perturbation strikes a second BIM core at a concave corner of the FF. d) The perturbation goes to infinity along a BIM core that stretches to infinity. Though the size of the perturbation could grow indefinitely, the perturbed front still returns to the FF pointwise.

a perturbation localized at some point \mathbf{r} of the FF that is not an SSS BFP. This perturbation will be “swept” along the front, away from the unstable BFP that generates the BIM; the perturbation might even initially grow in size. The localized perturbation will continue to follow the BIM segment from which it was perturbed, and will subsequently encounter either an SSS point, a domain wall, another BIM segment of the FF, or it will be swept to infinity (Fig. 27). In the initial three cases, it is clear that the perturbation will disappear as it either shrinks into the SSS BFP (Fig. 27a), strikes the wall (Fig. 27b), or runs into the already burned region (Fig. 27c), assuming the initial size of the perturbation $\epsilon(\mathbf{r})$ is sufficiently small. The case in which the perturbation is swept to infinity (Fig. 27d) requires an additional assumption on the far field nature of the fluid flow, addressed in Sec. C 4.

Appendix C: Dynamics at infinity

In this paper, we assume that the fluid velocity field $\mathbf{u}(\mathbf{r})$ is smooth and either (i) has a bounded stream function or (ii) is “localized” with a simple far-field behavior.

More precisely, case (i) assumes that $\mathbf{u}(\mathbf{r})$ is generated by a stream function $\Psi(\mathbf{r})$ that has a global maximum and minimum over the fluid domain. This case applies, for example, to the stream function in Eq. (4), since in our restricted domain y is bounded between 0 and 1. Under case (i), no sliding front may be infinitely long without striking a SZ, since a sliding front element increases or decreases its stream function value at the constant rate v_0 , Eq. (A13). Thus, for case (i) there are no BIM cores that stretch all the way to infinity.

The remainder of this appendix concerns case (ii),

stated more precisely as the requirement that, as r goes to infinity, $\mathbf{u}(\mathbf{r})$ behaves as a homogeneous polynomial $\mathbf{P}^k(x, y)$ of power $k \geq 0$ in the variables (x, y) , i.e.

$$\mathbf{u}(\mathbf{r}) = \mathbf{P}^k(x, y) + \mathbf{E}(x, y), \quad (\text{C1})$$

where $\mathbf{E}(x, y)$ is a term that grows more slowly than r^k . More precisely, we require that

$$\lim_{r \rightarrow \infty} r^{-k} \mathbf{E}(r \cos \phi, r \sin \phi) = 0, \quad (\text{C2})$$

with the polar angle ϕ held constant in the limit. Furthermore, we require that radial derivatives of \mathbf{E} grow more slowly, according to

$$\lim_{r \rightarrow \infty} r^{-k+\ell} \frac{\partial^\ell}{\partial r^\ell} \mathbf{E}(r \cos \phi, r \sin \phi) = 0, \quad 0 \leq \ell. \quad (\text{C3})$$

This assumption on the far field behavior eliminates, for example, infinite arrays of vortices [though such arrays could be allowed under case (i)], while allowing many important cases, including flows with constant far field velocities, linear hyperbolic and elliptic flows, other polynomial flows, and flows constructed from arbitrary configurations of a finite number of vortices.

1. Existence criteria for fixed points at infinity

By a burning fixed point “at infinity”, we intuitively mean a front element trajectory that attains a constant orientation θ and polar angle ϕ at an infinite value of r . We can formalize this definition by adapting the standard Poincaré compactification of the plane [41]. First, map the radial distance r , $0 \leq r < \infty$, to a new radial variable ρ , $0 \leq \rho < \pi/2$, defined by

$$\rho = \arctan r. \quad (\text{C4})$$

Similarly, introduce scaled Cartesian coordinates $\boldsymbol{\rho} = (\rho_x, \rho_y) = (x, y)\rho/r$. This transformation maps the xy -plane to an open disk of radius $\pi/2$ in the $\boldsymbol{\rho}$ -plane. We then include in our phase space the boundary of the disk at $\rho = \pi/2$, representing the “circle at infinity”. Equation (C4) yields

$$\dot{\boldsymbol{\rho}} = \frac{\rho}{\tan \rho} (\mathbf{I} - \hat{\boldsymbol{\rho}} \otimes \hat{\boldsymbol{\rho}}) \dot{\mathbf{r}} + (\cos^2 \rho) (\hat{\boldsymbol{\rho}} \otimes \hat{\boldsymbol{\rho}}) \dot{\mathbf{r}} \quad (\text{C5})$$

$$= \frac{\rho}{\tan \rho} (\mathbf{I} - \hat{\boldsymbol{\rho}} \otimes \hat{\boldsymbol{\rho}}) (\mathbf{u} + v_0 \hat{\mathbf{n}}) + (\cos^2 \rho) (\hat{\boldsymbol{\rho}} \otimes \hat{\boldsymbol{\rho}}) (\mathbf{u} + v_0 \hat{\mathbf{n}}), \quad (\text{C6})$$

where the second equality follows from Eq. (2a). Here, \mathbf{I} is the identity matrix and $\hat{\boldsymbol{\rho}} \otimes \hat{\boldsymbol{\rho}}$ is the tensor product with components $(\hat{\boldsymbol{\rho}} \otimes \hat{\boldsymbol{\rho}})_{ij} = \rho_i \rho_j / \rho^2$. Equation (C6) is smooth in (ρ_x, ρ_y, θ) everywhere except possibly at the boundary $\rho = \pi/2$.

Note that Eq. (C1) can be reexpressed in (ρ, ϕ) coordinates as

$$\mathbf{u}(\rho, \phi) = \cos^{-k}(\rho) \mathbf{Q}(\phi) + \bar{\mathbf{E}}(\rho, \phi), \quad (\text{C7})$$

where \mathbf{Q} is smooth in ϕ and where

$$\lim_{\rho \rightarrow \pi/2} \cos^{k-\ell}(\rho) \frac{\partial^\ell}{\partial \rho^\ell} \bar{\mathbf{E}}(\rho, \phi) = 0, \quad 0 \leq \ell, \quad (\text{C8})$$

with fixed ϕ . Thus as ρ goes to $\pi/2$, Eq. (C6) scales as $1/\cos^{k-1} \rho$, and is thereby singular for $k > 1$. To remove this singularity, the ODE time-parameter t can be replaced by a new scaled parameter s defined by

$$\frac{ds}{dt} = \frac{1}{\cos^{k-1} \rho}, \quad k \geq 1. \quad (\text{C9})$$

When $k = 0$, we make no scaling. This yields

$$\begin{aligned} \frac{d}{ds} \boldsymbol{\rho} &= \frac{\rho \cos^k \rho}{\sin \rho} (\mathbf{I} - \hat{\boldsymbol{\rho}} \otimes \hat{\boldsymbol{\rho}}) (\mathbf{u} + v_0 \hat{\mathbf{n}}) \\ &+ (\cos^{k+1} \rho) (\hat{\boldsymbol{\rho}} \otimes \hat{\boldsymbol{\rho}}) (\mathbf{u} + v_0 \hat{\mathbf{n}}), \quad k \geq 1. \end{aligned} \quad (\text{C10})$$

The right-hand side of Eq. (C10) is now smooth over the entire closed disk $\rho \leq \pi/2$ and all θ values, except possibly at $\rho = 0$, which does not concern us since our focus is at $\rho = \pi/2$. One can also see that

$$\frac{d}{ds} \theta = -(\cos^{k-1} \rho) \hat{n}_i u_{i,j} \hat{g}_j, \quad k \geq 1, \quad (\text{C11})$$

is smooth in (ρ_x, ρ_y, θ) for all $\rho < \pi/2$, but might be singular at $\rho = \pi/2$.

We define a fixed point at infinity of Eq. (2) to be a fixed point $(\rho_x^*, \rho_y^*, \theta^*)$ at $\rho^* = \pi/2$ for Eqs. (C10) and (C11) ($k \geq 1$) or Eqs. (C5) and (2b) ($k = 0$). We next restrict attention to those fixed points at infinity that are the limits of sliding fronts extending to infinity. The tangent direction of a sliding front that converges upon a fixed point at infinity must thus converge to $\pm \hat{\boldsymbol{\rho}}$. Thus, such a fixed point must yield

$$\hat{\mathbf{g}}^* = \pm \hat{\boldsymbol{\rho}}, \quad (\text{C12})$$

$$\lim_{r \rightarrow \infty} \frac{\dot{\mathbf{r}}^2}{|\dot{\mathbf{r}}|^2} = 1. \quad (\text{C13})$$

Furthermore, notice that at $\rho = \pi/2$, the term $(\cos^{k-1} \rho) u_{i,j} \hat{g}_j$ in Eq. (C11) will be noninfinite if $\hat{\mathbf{g}} = \pm \hat{\boldsymbol{\rho}}$ [see Eqs. (C7) and (C8)], a fortuitous consequence of searching for fixed points that are the limits of sliding fronts.

Equation (C13) can be rewritten as

$$1 = \lim_{r \rightarrow \infty} \frac{(u_r + v_0 \hat{n}_r)^2}{|\mathbf{u} + v_0 \hat{\mathbf{n}}|^2} = \lim_{r \rightarrow \infty} \frac{u_r^2}{|\mathbf{u} \pm v_0 \hat{\boldsymbol{\phi}}|^2} \quad (\text{C14})$$

$$= \lim_{\rho \rightarrow \pi/2} \frac{\cos^{-2k}(\rho) Q_r^2(\phi)}{\cos^{-2k}(\rho) Q_r^2(\phi) + [\cos^{-k}(\rho) Q_\phi(\phi) \pm v_0]^2} \quad (\text{C15})$$

$$= \lim_{\rho \rightarrow \pi/2} \frac{Q_r^2(\phi)}{Q_r^2(\phi) + [Q_\phi(\phi) \pm v_0 \cos^k(\rho)]^2}, \quad (\text{C16})$$

where the second equality follows from Eq. (C12) and the third from Eqs. (C7) and (C8). This implies that for a

fixed point at infinity (that is the limit of a sliding front) in polar coordinates $(\pi/2, \phi^*, \theta^*)$

$$Q_\phi(\phi^*) = \pm v_0 \cos^k(\pi/2) = \begin{cases} \pm v_0 & \text{if } k = 0, \\ 0 & \text{if } k \geq 1. \end{cases} \quad (\text{C17})$$

Assume now that $k \geq 1$. We seek necessary and sufficient conditions for $d\boldsymbol{\rho}/ds = 0$ at $\rho = \pi/2$. Equations (C7), (C8), and (C10) imply that at $\rho = \pi/2$

$$\frac{d}{ds}\boldsymbol{\rho}(\pi/2, \phi, \theta) = \frac{\pi}{2}(1 - \hat{\boldsymbol{\rho}} \otimes \hat{\boldsymbol{\rho}})\mathbf{Q}(\phi) = \frac{\pi}{2}\hat{\phi}Q_\phi(\phi), \quad (\text{C18})$$

which is independent of θ . Thus, a necessary and sufficient condition for $d\boldsymbol{\rho}/ds = 0$ at $\rho = \pi/2$ is

$$Q_\phi(\phi^*) = 0, \quad k \geq 1, \quad (\text{C19})$$

consistent with the sliding front condition Eq. (C17).

We now seek necessary and sufficient conditions for $d\theta/ds = 0$. Based on Eq. (C11), we define the scaled Jacobian matrix

$$\mathbf{J}(\rho, \phi) = \cos^{k-1}\rho \begin{bmatrix} u_{r,r} & u_{r,\phi}/r \\ u_{\phi,r} & u_{\phi,\phi}/r \end{bmatrix} \quad (\text{C20})$$

expressed in the $(\hat{\mathbf{r}}, \hat{\phi})$ basis. Under assumptions (C7) and (C8), one can show that \mathbf{J} takes on the following form at $\rho = \pi/2$.

$$\mathbf{J}(\pi/2, \phi) = \begin{bmatrix} kQ_r(\phi) & Q_{r,\phi}(\phi) \\ kQ_\phi(\phi) & Q_{\phi,\phi}(\phi) \end{bmatrix}. \quad (\text{C21})$$

For a fixed point at $\rho = \pi/2$, we apply Eq. (C19) to obtain

$$\mathbf{J}(\pi/2, \phi^*) = \begin{bmatrix} kQ_r(\phi^*) & Q_{r,\phi}(\phi^*) \\ 0 & Q_{\phi,\phi}(\phi^*) \end{bmatrix}. \quad (\text{C22})$$

Setting $d\theta/ds = 0$ in Eq. (C11) is equivalent to $\hat{\mathbf{g}}$ being an eigenvector of \mathbf{J} . From Eqs. (C12) and (C22), however, we see that $\hat{\mathbf{g}} = \hat{\boldsymbol{\rho}}$ is already guaranteed to be an eigenvector of $\mathbf{J}(\pi/2, \phi^*)$. Thus, $d\theta/ds = 0$ is already implied by Eqs. (C12) and (C19).

Assume now that $k = 0$. Then $\mathbf{P}^k(x, y)$ is constant, and it is easy to see from Eq. (C6) and Eq. (2b) that $\dot{\boldsymbol{\rho}} = 0$ and $\dot{\theta} = 0$ at $\rho = \pi/2$ for any ϕ and θ . However, ϕ and θ are no longer arbitrary when we apply the sliding front conditions Eq. (C12) and Eq. (C17).

To summarize, we have the following conditions on the existence of fixed points at infinity.

Theorem 2. *Assume the incompressible flow \mathbf{u} satisfies Eqs. (C1) and (C3) or equivalently Eqs. (C7) and (C8). Then a sliding front ends in a fixed point at infinity with orientation and position angles θ^* and ϕ^* if and only if $\hat{\mathbf{g}}(\theta^*) = \pm \hat{\boldsymbol{\rho}}(\phi^*)$ and*

$$Q_\phi(\phi^*) = 0, \text{ for } k \geq 1, \quad (\text{C23})$$

$$Q_\phi(\phi^*) = \pm v_0, \text{ for } k = 0. \quad (\text{C24})$$

2. Stability of fixed points at infinity

Assume $k \geq 1$. To determine the stability of fixed points at infinity, we compute the Jacobian matrix of the flow (C10) and (C11) in (ρ, ϕ, θ) coordinates, i.e.

$$\mathcal{J} = \frac{\partial(\rho', \phi', \theta')}{\partial(\rho, \phi, \theta)}. \quad (\text{C25})$$

Applying the results of Theorem 2, it can be shown that the Jacobian at a fixed point at infinity (to which a sliding front converges) is

$$\mathcal{J} = \begin{bmatrix} -Q_r & 0 & 0 \\ \phi'_{,\rho} & Q_{\phi,\phi} & 0 \\ 0 & kQ_{\phi,\phi} & Q_{\phi,\phi} - kQ_r \end{bmatrix}, \quad (\text{C26})$$

where

$$\phi'_{,\rho} = -k(\cos \rho)^{k-1}(\bar{E}_\phi + v_0 \hat{n}_\phi). \quad (\text{C27})$$

Applying the area-preservation constraint $\nabla \cdot \mathbf{u} = 0$ to Eqs. (C7) and (C8), we find

$$Q_{\phi,\phi} = -(1+k)Q_r, \quad (\text{C28})$$

from which

$$\mathcal{J} = \begin{bmatrix} -Q_r & 0 & 0 \\ \phi'_{,\rho} & -(1+k)Q_r & 0 \\ 0 & -(1+k)kQ_r & -(1+2k)Q_r \end{bmatrix}. \quad (\text{C29})$$

Thus, the eigenvalues of \mathcal{J} all have the same sign, which is the opposite sign to Q_r . We thus have the following.

Theorem 3. *Assume the incompressible flow \mathbf{u} satisfies Eqs. (C1) and (C3), with $k \geq 1$. Suppose a sliding front ends in a fixed point $(\pi/2, \phi^*, \theta^*)$ at infinity and assume $Q_r(\phi^*) \neq 0$. Then the fixed point has stability SSS (UUU) if the flow along the sliding front is radially outward (inward), i.e. $Q_r(\phi^*) > 0$ ($Q_r(\phi^*) < 0$).*

In the $k = 0$ case, the eigenvalues of the Jacobian are all 0, and stability must be determined by nonlinear analysis.

3. Behavior of frozen fronts at infinity

Consider a sliding front that extends to infinity without containing a cusp beyond some set radius. Such a front must be a trajectory of the \mathbf{w}_\pm field Eq. (A3) with a single choice of sign. Transforming this vector field into the $\boldsymbol{\rho}$ -coordinates according to Eq. (C5) and scaling time via Eq. (C9), we obtain a smooth 2D vector field over $\boldsymbol{\rho}$ -space in the neighborhood of the boundary $\rho = \pi/2$. Thus the sliding front that extends to infinity, i.e. converges to $\rho = \pi/2$ in the $\boldsymbol{\rho}$ -coordinates, can do only one of two things. If the boundary $\rho = \pi/2$ contains no

fixed point, then the boundary is a limit cycle to which the sliding front converges. Otherwise, the sliding front must converge upon a fixed point at $\rho = \pi/2$.

Let us suppose that the boundary $\rho = \pi/2$ is a limit cycle, which we also suppose is stable. (The analysis of the unstable case is similar.) Then, a circle at $\rho = \pi/2 - \epsilon$ will converge outward to $\pi/2$ for a small enough ϵ . In the original xy -coordinates, this means that a large enough circle of front elements would expand outward without bound. If these front elements were passive tracers of the flow, this outward expansion would clearly violate conservation of area of the underlying flow. Similarly, if these front elements were all pointing inward with nonzero v_0 , they would clearly still violate conservation of area of the underlying flow. Thus, the front elements can only be facing outward if the circle is ultimately to grow in size. In summary, we have the following.

Proposition 2. *Assume the incompressible flow \mathbf{u} satisfies Eqs. (C1) and (C3). A sliding front that moves outward to (inward from) infinity, without cusps beyond a certain radius, with its burning direction pointed inward (outward) must converge upon a fixed point $(\pi/2, \phi^*, \theta^*)$ at infinity.*

Consider now a frozen front that converges on a limit cycle at infinity. There would in fact need to be two separate frozen fronts converging upon a limit cycle at infinity, one burning inward and one burning outward, to create a burned strip that spirals outward to infinity. However, the previous proposition shows that only one such burning direction is possible. Hence, we have shown the following.

Proposition 3. *Assume the incompressible flow \mathbf{u} satisfies Eqs. (C1) and (C3). Any frozen front that extends to infinity, without any concave corners or BFPs beyond a certain radius, must be a sliding front converging upon a fixed point at infinity.*

4. Stability of frozen fronts extending to infinity

We now complete the discussion of frozen front stability begun in Appendix B. In particular we consider a FF F that extends to infinity and an allowable perturbation to F at a point $\mathbf{r} \in F$ that is, at least initially, swept toward infinity. Our concern is that this perturbation may not only grow in time, but could burn far enough away from F that it would no longer be carried away to infinity but would leave some new part of the fluid, not in the original burned domain defined by F , burned forever. This problem is resolved, however, by the Poincaré compactification. If the sliding front converges on a stable fixed point at $\rho = \pi/2$, then one can always find a sufficiently small perturbation $\epsilon(\mathbf{r})$ such that the perturbation never grows too large to be collapsed by the SSS BFP at infinity.

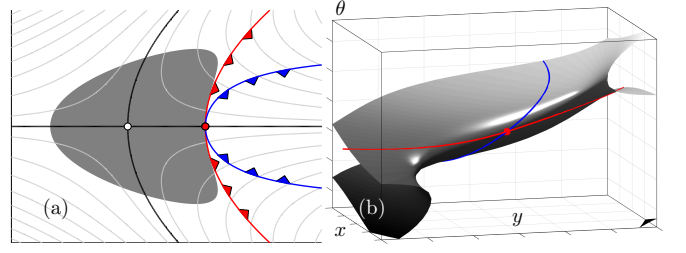


FIG. 28. (Color online.) When the parameter c is below 2, the curvature of the SZ is not strong enough to create the SSU to SSU-SSS-SSU bifurcation. ($v_0 = 1, \mu = 1, c = 7/4$). (a) SSU BFP with attached sliding fronts. Three other BFPs on the SZ boundary are not shown. (b) Fronts on the sliding surface seen in 3D from the center of the SZ.

Appendix D: SSS points

It was shown in Ref. [8] that SSS is a possible stability type for BFPs. Here we provide an explicit example for the fluid flow surrounding an SSS point.

The stream function

$$\Psi = -v_0 y - \mu xy + \frac{c\mu^2}{6v_0} y^3 \quad (\text{D1})$$

produces the following flow field with a BFP at $(x, y) = (0, 0)$ and $\hat{\mathbf{g}} = \hat{\mathbf{y}}$

$$u_x = -v_0 - \mu x + \frac{c\mu^2}{2v_0} y^2, \quad (\text{D2})$$

$$u_y = \mu y, \quad (\text{D3})$$

where v_0 is the burning speed, μ is the eigenvalue from Eq. (A4), and c is a new parameter. Note that this flow can be understood as the combination of a uniform “wind”, a linear hyperbolic flow, and a Poiseuille flow. The stability of the BFP can be determined from Theorem 1 once μ' is computed. Ref. [8], Eqs. (19) and (31), showed that

$$\mu' = (2\mu^2 - v_0 \mathbf{a} \cdot \mathbf{g})/\mu, \quad (\text{D4})$$

$$\mathbf{a} \cdot \mathbf{g} = n_i g_j g_k u_{i,j,k}, \quad (\text{D5})$$

from which it is straightforward to compute $\mathbf{a} \cdot \mathbf{g} = c\mu^2/v_0$ and $\mu' = (2 - c)\mu$. Thus, the BFP at the origin has stability SSS if $\mu > 0$ and $c > 2$. If in addition $c \leq 9/4$, Eqs. (A6) and (A7) show that the three eigenvalues are real.

Figure 28 illustrates this flow for $c = 7/4$, which is too small to produce an SSS BFP at the origin. Equation (A5) allows us to interpret this fact as due to the magnitude of the SZ curvature $|\kappa|$ being too small. Topologically, the dynamics has the same structure as the linear hyperbolic flow Fig. 23, since the origin is an SSU BFP. The BIM (red) forms a FF extending to infinity.

Increasing c to $8.5/4$, the magnitude of the SZ curvature at the BFP is increased (Fig. 29). The SSU BFP in

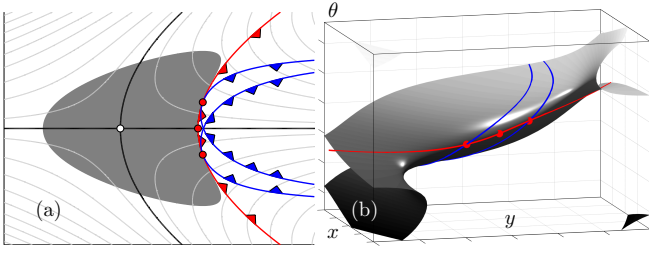


FIG. 29. (Color online.) ($v_0 = 1, \mu = 1, c = 8.5/4$). (a) When the central SSS BFP has real eigenvalues, the BIMs emanating from the two neighboring SSU BFPs reach it with no cusps. (b) BIMs run very close to the sliding surface fold.

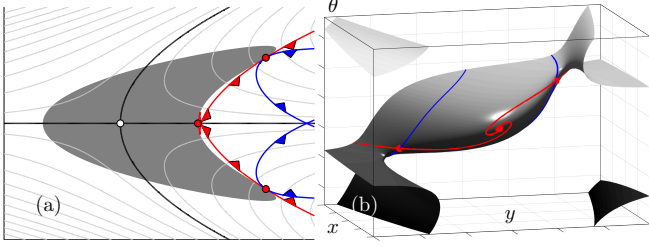


FIG. 30. (Color online.) ($v_0 = 1, \mu = 1, c = 15/4$). (a) When the central SSS BFP has complex eigenvalues, the BIMs emanating from the SSU BFPs repeatedly overshoot the SSS BFP, and form cusps. (b) From side view, it is clear that these cusps are caused by the local spiraling of trajectories.

Fig. 28 has bifurcated into an SSS BFP at the origin sur-

rounded by two SSU BFPs. The BIMs emanating from the SSU BFPs toward the central SSS BFP actually terminate on the SSS BFP (most easily seen in Fig. 29b.) Thus, all three BFPs lie on the FF composed of these BIMs.

Increasing c further to $15/4$, the SSS point acquires complex eigenvalues. Therefore, any sliding trajectory that reaches the center point must first encircle it an infinite number of times (Fig. 30). Because the SSS point is on the fold of the sliding surface (where $|\mathbf{u}| = v_0$), such a trajectory must pass through the fold an infinite number of times, generating an infinite sequence of cusps. Therefore, for any point along a sliding trajectory (which we imagine to be a part of some FF), there must exist an infinite number of cusps between it and the SSS point. This ensures that an SSS point with complex eigenvalues cannot lie on a FF.

Conversely, an SSS point can only lie on a FF if its eigenvalues are real. Such SSS points do exist in the flow Eq. (D2) for parameters satisfying $v_0 > 0, \mu > 0, 8/4 < c < 9/4$. Thus in Fig. 29 the real eigenvalues ensure that the SSS point lies on the FF attached to the neighboring SSU points. Because the eigenvalues are real for an open interval in parameter space, the connection between the SSU and SSS BFPs in Fig. 29 is structurally stable. Here the FF runs very close to the SZ boundary, however there is a small gap. Contrast this with the SSU to SSU connection previously shown in Fig. 13, which was not structurally stable.

-
- [1] T. John and I. Mezic, *Phys. Fluids*, **19** (2007).
 - [2] D. Beule, A. Forster, and T. Fricke, *Int. J. Research Phys. Chem. and Chem. Phys.*, **204**, 1 (1998).
 - [3] A. Scotti and J. Pineda, *J. Marine Res.*, **65**, 117 (2007).
 - [4] I. Prigogine and I. Stengers, *Order Out of Chaos: Man's New Dialogue with Nature* (Bantam, New York, 1984).
 - [5] A. Babloyantz, *Molecular Dynamics and Life: An Introduction to Self-Organization of Matter* (Wiley, New York, 1986).
 - [6] C. A. Russell, D. L. Smith, L. A. Waller, J. E. Childs, and L. A. Real, *Proc. Roy. Soc. London Ser. B – Biol. Sci.*, **271**, 21 (2004).
 - [7] J. Mahoney, D. Bargteil, M. Kingsbury, K. Mitchell, and T. Solomon, *Euro. Phys. Lett.*, **98**, 44005 (2012).
 - [8] K. A. Mitchell and J. Mahoney, *Chaos*, **22** (2012), ISSN 10541500, doi:10.1063/1.4746039.
 - [9] D. Bargteil and T. Solomon, *Chaos*, **22** (2012), ISSN 10541500, doi:10.1063/1.4746764.
 - [10] M. E. Schwartz and T. H. Solomon, *Phys. Rev. Lett.*, **100**, 028302 (2008).
 - [11] S. Chandrasekhar, *Hydrodynamic and Hydromagnetic Stability* (Clarendon, Oxford, 1961).
 - [12] R. M. Clever and F. H. Busse, *J. Fluid Mech.*, **65**, 625 (1974).
 - [13] E. W. Bolton, F. H. Busse, and R. M. Clever, *J. Fluid Mech.*, **164**, 469 (1986).
 - [14] T. H. Solomon and J. P. Gollub, *Phys. Rev. A*, **38**, 6280 (1988).
 - [15] M. C. Cross and P. C. Hohenberg, *Rev. Mod. Phys.*, **65**, 851 (1993).
 - [16] D. Etling and R. A. Brown, *Boundary-Layer Meteor.*, **65**, 215 (1993).
 - [17] B. W. Atkinson and J. W. Zhang, *Rev. Geophys.*, **34**, 403 (1996).
 - [18] B. Shraiman, *Phys. Rev. A*, **36**, 1374 (1987).
 - [19] T. Solomon and J. Gollub, *Phys. Fluids*, **31**, 1372 (1988).
 - [20] R. Camassa and S. Wiggins, *Phys. Rev. A*, **43**, 774 (1991).
 - [21] T. H. Solomon, S. Tomas, and J. L. Warner, *Phys. Rev. Lett.*, **77**, 2682 (1996).
 - [22] M. Abel, A. Celani, D. Vergni, and A. Vulpiani, *Phys. Rev. E*, **64**, 046307 (2001).
 - [23] M. Abel, M. Cencini, D. Vergni, and A. Vulpiani, *Chaos*, **12**, 481 (2002), ISSN 10541500.
 - [24] M. Cencini, A. Torcini, D. Vergni, and A. Vulpiani, *Phys. Fluids*, **15**, 679 (2003), ISSN 10706631.
 - [25] M. S. Paoletti and T. H. Solomon, *Euro. Phys. Lett.*, **69**, 819 (2005).
 - [26] M. S. Paoletti and T. H. Solomon, *Phys. Rev. E*, **72**, 046204 (2005).
 - [27] J. R. Boehmer and T. H. Solomon, *Euro. Phys. Lett.*, **83**, 58002 (2008).

- [28] S. K. Scott, *Oscillations, Waves, and Chaos in Chemical Kinetics* (Oxford University Press, Oxford, 1994).
- [29] A. Pocheau and F. Harambat, Phys. Rev. E, **73**, 065304 (2006).
- [30] A. Pocheau and F. Harambat, Phys. Rev. E, **77**, 036304 (2008).
- [31] There are small variations in the propagation speed due to curvature of the reaction front, but this effect is minimal in these experiments.
- [32] The experiment presented here depends on a redox reaction, and in this spirit we use the term “burning” to refer to any similar form of front propagation.
- [33] These frozen domains are similar to the minimal forward invariant sets studied in the context of random differential equations with bounded noise [42, 43].
- [34] T. H. Solomon and I. Mezić, Nature, **425**, 376 (2003).
- [35] E. Hernandez-Garcia and C. Lopez, Ecol. Complexity, **1**, 253 (2004).
- [36] M. Kaern and M. Menzinger, J. Phys. Chem. B, **106**, 3751 (2002).
- [37] S. Saha, S. Atis, D. Salin, and L. Talon, Europhys. Lett., **101**, 38003 (2013).
- [38] P. W. Megson, M. L. Najarian, K. E. Lilienthal, and T. H. Solomon, Phys. Fluids, **27**, 023601 (2015).
- [39] Interestingly, these two sliding surfaces are related by $x \leftrightarrow y$ symmetry.
- [40] We correct a typo in the original: in the bottom row of the table, $\mu' > 0$ now reads $\mu' < 0$.
- [41] L. Perko, *Differential Equations and Dynamical Systems* (Springer, New York, 2001).
- [42] A. J. Homburg and T. R. Young, Topol. Methods Nonlinear Analysis, **35**, 77 (2010).
- [43] J. S. W. Lamb, M. Rasmussen, and C. S. Rodrigues, to appear in: Proceedings of the American Mathematical Society (2014), <http://arxiv.org/abs/1105.5018>.